

TITLE OF JIM HENEGHAN'S THESIS

by

DERMOT (JIM) HENEGHAN

(Under the Direction of William Micheal Dennis)

ABSTRACT

TITLE OF JIM HENEGHAN'S THESIS

by

DERMOT (JIM) HENEGHAN

B.Sc., University of Limerick, 2008

M.Sc., University of Limerick, 2011

A Dissertation Submitted to the Graduate Faculty
of The University of Georgia in Partial Fulfillment
of the
Requirements for the Degree

DOCTOR OF PHILOSOPHY

ATHENS, GEORGIA

2021

TITLE OF JIM HENEGHAN'S THESIS

by

DERMOT (JIM) HENEGHAN

Approved:

Major Professor: William
Micheal Dennis

Committee: Heinz
Bernd Schuttler
Micheal
Geller

© 2021
Dermot (Jim) Heneghan
All Rights Reserved

Electronic Version Approved:

Ron Walcott
Dean of the Graduate School
The University of Georgia
May 2021

*Dedication

CONTENTS		iii
List of Tables	iii	5
List of Figures	iii	5
I. Chapters	2	5
II. Introduction	2	5
III. FDTD Overview	2	5
A. Generic explanation	2	5
B. Types of Analysis done with FDTD	2	5
C. Utility of FDTD	2	5
1. Limits of FDTD	2	5
IV. FDTD Adaptation	2	5
V. Sources	4	12
1. The Ricker Wavelet	4	12
A. Point Sources	4	12
B. TFSF Source	4	12
VI. Boundary Conditions	4	12
A. PEC Boundary	4	12
B. Periodic Boundary	4	12
1. Bloch Periodic Boundary	5	12
C. Perfectly Matched Layers	5	12
D. UPML	5	12
E. CPML	5	12
VII. Materials Models	5	12
A. Isotropy	5	12
1. Isotropic	5	12
2. Anisotropic	5	12
3. Diagonally Anisotropic	5	12
B. Dielectric Materials	5	12
C. Dispersive materials	5	12
1. Z Transform	5	12
2. Drude Model	5	12
3. Debye Drude Model	5	12
4. Lorentz	5	12
5. Diagonally Anisotropic	5	12
VIII. Sensors	5	12
A. Time domain sensors	5	12
B. Frequency Domain Sensors	5	12
1. Heat Maps	5	12
2. RTA Spectra	5	12
IX. Analysis Tools	5	12
A. Types	5	12
1. Spectral	5	12
2. Photonic Band	5	12
3. Dispersion	5	12
4. Heat Map	5	12
B. Imaging	5	12
C. Raster Dispersion	5	12
X. Other Methods	5	12
A. Transfer Matrix	5	12
XI. Introduction	5	12
XII. Results and Discussion	5	12
A. Far-Field Analysis	5	12
B. Near-Field Analysis	6	12
XIII. Introduction	11	12
XIV. Results and Discussion	12	12
XV. Conclusion	16	12
XVI. A Yet To Be Submitted Paper	17	12
XVII. Standard section	17	12
LIST OF TABLES		
LIST OF FIGURES		
1	Reflectance spectra for various thicknesses of hBN. The dots are digitized data from Caldwell <i>et al</i> ¹ , the dark solid lines are the spectra calculated using the transfer matrix method, the light solid lines are spectra calculated from FDTD simulations. note for Dr D. I intend to replace this figure with a 3 pane image. (a) will be the figure shown here but with one of the solid lines replaced with dashes and possibly one less thickness. Pane (b) will be the fitted curve that was used to calculate gamma. Pane (c) will be the FDTD and TMM RTA spectra. This section may be better placed in chapter 2	3

2	(Color online) Schematic of the hBN/Au structure simulated in this work. (a) Planar view at the hBN/Au interface. (b) Cross-sectional view. CPML: Convolutional perfectly matched layer boundary conditions are imposed at the z - direction boundaries. Periodic boundary conditions are imposed at the x and y boundaries. The unit cell lengths in the x - and y - directions are d_x and d_y , respectively. The layer thicknesses are $d_{\text{VAC}} = 0.87 \mu\text{m}$, $d_{\text{hBN}} = 80 \text{ nm}$, $d_{\text{SiO}_2} = 1.0 \mu\text{m}$, $d_{\text{Au}} = 50 \text{ nm}$. The length of the long segments of the cross pattern is $l = 0.8 d_x = 0.8 d_y$ while the width of the cross is $w = 0.15 d_x = 0.15 d_y$. The distance between the centers of neighboring crosses is $d_{\text{CC}} = d_x = d_y$. The directions of the \mathbf{E} -field, \mathbf{H} -Field and propagation vector \mathbf{k} are shown in both panes.	6
3	(Color online) (a) The absorptance spectrum of the BD for a range of d_{CC} values. (b) The absorptance spectra of the UCDI. (c) The absorptance spectra of the CD. The gray dotted curve in pane (c) depicts the absorption spectra for the UCDII with $d_{\text{CC}} = 3.14 \mu\text{m}$. The vertical black dashed lines in this figure indicate the position of the hBN TO and LO phonon frequencies as described in the main text.	7
4	(Color online) (a) Absorptance spectra for the UCDI vs the peak frequency of the BD (ν_{bare}) plotted as a color map. The symbols indicate the peaks in the absorptance spectra. The triangular symbols are due to Rayleigh anomalies, while the square symbols indicate the plasmon-polariton, which shifts linearly with ν_{bare} . (b) Absorptance spectra for the CD vs the peak frequency of the BD (ν_{bare}) plotted as a color map. The symbols indicate the peaks/shoulders in the absorptance spectra. The triangular symbols are due to Rayleigh anomalies, while the square symbols show the interaction between plasmon-polariton in the nanopatterned Au film and the bulk phonon-polariton in the hBN. The interpretation of the features labeled by the circular symbols are given in the main text.	7
5	(Color online) Background subtracted and normalized planar and cross-sectional colormaps of the field magnitude for the BD, UCDI, UCDII, and CD with $d_{\text{CC}} = 3.14 \mu\text{m}$. Panes (a) – (h) were excited below the restrahlen band at $\nu = 1200 \text{ cm}^{-1}$. The white lines in the planar colormaps panes (a) – (d) indicate the location of the cross-sectional colormaps in (e) – (h). Panes (i) – (p) were excited in the restrahlen band at $\nu = 1500 \text{ cm}^{-1}$. The white lines in the planar colormaps panes (i) – (l) indicate the location of the cross-sectional colormaps in (m) – (p). Panes (q) – (x) were excited above the restrahlen band at $\nu = 1700 \text{ cm}^{-1}$. The white lines in the planar colormaps panes (q) – (t) indicate the location of the cross-sectional colormaps in (u) – (x).	8
6	(Color online) (a) Lineouts of the magnitude of the electric field for a range of excitation frequencies in the restrahlen band $\nu = 1490 - 1570 \text{ cm}^{-1}$. The circular dots indicate peaks in the lineout. (b) Dispersion curve constructed from the peak data in pane (a). (c) Lineouts of the y -component of the electric field for a range of excitation frequencies in the restrahlen band $\nu = 1490 - 1570 \text{ cm}^{-1}$. The circular dots indicate peaks in the lineout. (d) Dispersion curve constructed from the peak data in pane (c). The inserts in panes (b) and (d) show the position of the lineouts in panes (a) and (c).	9
7	Simulational structure.	12
8	Dielectric function and resulting spectra of 80 nm hBN.	14
9	Absorptance spectra for devices simulated.	14
10	Rasterized frequency "heat maps" for coupled and uncoupled devices	15
11	Cross-sectional colormaps of the field components in both the hBN (coupled) devices and uncoupled devices at four representative frequencies	19
12	Experimental and simulational planar colormaps and their central lineout data.	20

Introduction

I. CHAPTERS

Methods

II. INTRODUCTION

Electromagnetic simulations in this dissertation were performed using the Finite-Difference Time-Domain (FDTD) method.

III. FDTD OVERVIEW

The Finite-Difference Time-Domain (FDTD) method is a technique for iteratively solving Maxwell's curl equations. Using the finite difference approximation, the equations are discretized for computational use and thus is second order accurate. The modern method for FDTD simulation, initially proposed by Yee in 1966 REF, constructs a grid is constructed where the electric field components are offset in space by half a grid dimension as can be seen in [FIGURE]. We call a single cell of this arrangement the *Yee Cell*. To calculate the electric field value at a grid point the simulation needs to know the value at that point one time step earlier and the magnetic field value in the surrounding grid points half a time step earlier. Thus, the simulation alternately calculates the entire magnetic field and in the simulation field before calculating the electric field one half time step later.

$$\begin{aligned} \nabla \times \mathbf{E} &= -\mu \frac{\partial \mathbf{H}}{\partial t} \\ \frac{\partial \mathbf{H}}{\partial t} &= -\frac{1}{\mu} \nabla \times \mathbf{E} \\ \frac{\mathbf{H}(t + \frac{\Delta t}{2}) - \mathbf{H}(t - \frac{\Delta t}{2})}{\Delta t} &= -\frac{1}{\mu} \nabla \times \mathbf{E}(t) \\ \mathbf{H}(t + \frac{\Delta t}{2}) &= \mathbf{H}(t - \frac{\Delta t}{2}) - \frac{\Delta t}{\mu} \nabla \times \mathbf{E}(t) \end{aligned}$$

These equations are then solved for each vector component

$$H_x(x, y, z)^{t+\frac{\Delta t}{2}} = H_x(x, y, z)^{t+\frac{\Delta t}{2}} - \frac{\Delta t}{\mu} \left(\frac{E_y^t(x, y + 1, z) - E_y^t(x, y - 1, z)}{\Delta y} \right) \quad (2)$$

where x, y, z represent coordinates in simulation space, $\Delta x, \Delta y, \Delta z$ are the lengths of the Yee cell in that dimension and Δt is the simulation time step. As can be seen in (1) and (2) these formulations of Maxwell's curl equations are second order accurate. It has been shown

that to maintain numerical stability the ratio of the time step to spatial step must satisfy the condition $c\Delta t \leq \frac{1}{\Delta x^2 + \Delta y^2 + \Delta z^2}$. The maximum value, $S_c = \frac{c\Delta t}{\Delta x^2 + \Delta y^2 + \Delta z^2}$, is known as the *Courant number* [REF].

A. Generic explanation

The time domain nature of FDTD means that multiple frequencies of interest can be studied from a single simulation by using a broad band source. In this dissertation frequency domain analysis is performed with the FDTD code to produce electric field colormaps for a range of frequencies, reflectance and transmittance spectra and photonic band diagrams.

B. Types of Analysis done with FDTD

C. Utility of FDTD

The purpose of a FDTD simulation is to determine the electromagnetic response of some material structure. While simple methods for determining the response of layered structures, such as the transfer matrix method (TMM) [REF], are effective, FDTD has the added flexibility to simulate more complexly patterned structures. The time domain nature of FDTD, unlike its frequency domain counterparts, allows for broad band simulation while also allowing for the portrayal of specific frequency responses in post processing analysis. The method is accurate, robust and scalable. FDTD has been used to simulate macro scale objects, such as low visibility aircraft, scattering radar waves, cell phone signals interacting with human brain tissue and nano scale structures interacting with infrared wavelengths, which is the subject matter of this dissertation. Furthermore FDTD naturally handles nonlinear behavior, can handle anisotropic media and is easily parallelizable.

$$\frac{\mathbf{E}(t + \Delta t) - \mathbf{E}(t)}{\Delta t} = \frac{1}{\varepsilon} \nabla \times \mathbf{H}(t + \frac{\Delta t}{2})$$

$$\mathbf{E}(t) \xrightarrow{\text{limits of FDTD}} \frac{\Delta t}{\varepsilon} \nabla \times \mathbf{H}(t + \frac{\Delta t}{2}) \quad (1)$$

IV. FDTD ADAPTATION

For all simulations performed a broadband, plane wave source was used. The time profile of the source was a Ricker wavelet² centered on $\lambda = 2.4 \mu\text{m}$ (4167 cm^{-1}). This source excited a lateral Au layer in time pulse using the total-field scattered-field (TFSF) interface³. The source was y -polarized and propagated in the negative z -direction. The use of the TFSF method enabled sensors to be placed above the TFSF boundary in order to record only the reflected field values.

To prevent divergence in the simulation caused by edge reflections in the patterned Au layer, a convolutional perfectly matched layer (CPML)⁴ boundary was used as the

CPML has been shown to be more stable than a uniaxial perfectly matching layer (UPML)⁵ absorbing boundary for simulations of this kind. Periodic boundary conditions were used in the transverse directions. In the positive and negative z -directions, the simulation was terminated by 50 perfectly matched layers. Due to the difference between the length scales of features in the transverse and longitudinal directions, the computational grid used cell sizes in the ratio of 10:10:1 in the x -, y - and z -dimensions, respectively. The resonance frequency of the patterned Au layer was found to be sensitive to the spatial resolution used in the simulation. Convergence testing was performed and a working resolution of $\Delta x = 20 \text{ nm}$, $\Delta y = 20 \text{ nm}$, $\Delta z = 2 \text{ nm}$ was selected to be a good compromise between simulation accuracy and GPU memory limits.

Reflectance and transmittance spectra were calculated by means of planar Poynting vector monitors which calculated frequency resolved components of the Poynting vector. The frequency resolved field components were calculated “on the fly” using a discrete Fourier-transform (DFT) in the time domain. The Poynting vector was calculated from the field components using a plane wave expansion as detailed in Ref.⁶. The incident field data required to normalize the results were similarly calculated. The individual components of the spectrally resolved electric field in a given plane (*e.g.*, at the vacuum/hBN interface) could be output for further analysis and visualization.

The various components of the device were modelled as follows. The hBN layer was simulated using a tensor Lorentz model, *i.e.*,

$$\epsilon_{\text{hBN}}(\omega) = \begin{pmatrix} \epsilon_x(\omega) & 0 & 0 \\ 0 & \epsilon_y(\omega) & 0 \\ 0 & 0 & \epsilon_z(\omega) \end{pmatrix}, \quad (3)$$

where

$$\epsilon_k(\omega) = \epsilon_k(\infty) + \frac{S_k \omega_k^2}{\omega_k^2 - i\gamma_k \omega - \omega^2}, \quad (4)$$

$\epsilon_k(\infty)$ is the k^{th} component (where $k = x, y, z$) of the dielectric function at infinity, ω_k is the frequency of a transverse optical phonon propagating in the k^{th} direction, the factor $S_k \omega_k^2$ can be written in the form $\epsilon_k(\infty)(\omega_{\text{LO}}^2 - \omega_{\text{TO}}^2)^7$, showing the explicit dependence on the longitudinal optical (LO) and transverse optical (TO) phonon frequencies. Given the polarization of the excitation source (see Fig. 7) the in-plane parameters used in this research were $\epsilon_{x,y}(\infty) = 4.87$, $S_{x,y} = 0.61$, $\hbar\omega_{x,y} = 170.1 \text{ meV}$. The out-of-plane parameters were $\epsilon_z(\infty) = 2.95$, $S_z = 0.61$, $\gamma_z = 0.25 \text{ meV}$, and $\hbar\omega_z = 92.5 \text{ meV}$ from Ref.⁸. The notable exception was the planar damping constant $\gamma_{x,y}$, which has been shown to have a strong thickness dependence by Caldwell *et al.*¹. Using results from the Caldwell group, as detailed in the supplemental materials section of that

paper, the appropriate value of $\gamma_{x,y}$ for a film thickness of 80 nm was found to be 3.97 meV.

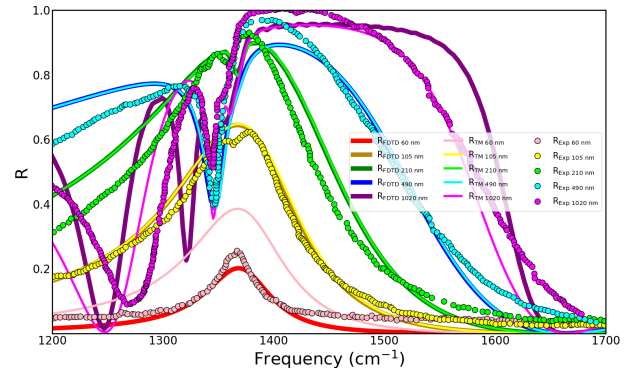


FIG. 1: Reflectance spectra for various thicknesses of hBN. The dots are digitized data from Caldwell *et al.*¹, the dark solid lines are the spectra calculated using the transfer matrix method, the light solid lines are spectra calculated from FDTD simulations. note for Dr D. I intend to replace this figure with a 3 pane image. (a) will be the figure shown here but with one of the solid lines replaced with dashes and possibly one less thickness. Pane (b) will be the fitted curve that was used to calculate gamma. Pane (c) will be the FDTD and TMM RTA spectra. This section may be better placed in chapter 2

The Au film was simulated using wavelength dependent refractive index data as detailed by Ciesielski *et al.*⁹ to fit to a Debye/Drude model, *i.e.*,

$$\epsilon_{\text{Au}}(\omega) = \epsilon_\infty + \frac{\epsilon_s - \epsilon_\infty}{1 + i\omega\tau_0} + \frac{\sigma}{i\omega\epsilon_0}, \quad (5)$$

where $\epsilon_\infty = 3.231$ is the dielectric function at infinity, $\epsilon_s = -1.598 \times 10^4$ is the static dielectric constant, $\tau_0 = 1.425 \times 10^{-14} \text{ s}$ is the relaxation constant and $\sigma = 1.006 \times 10^6 \text{ S m}^{-1}$ is the conductivity of Au, respectively. ϵ_0 is the permittivity of free space. Finally, the SiO₂ substrate was simulated using a simple dielectric with $\epsilon_{\text{SiO}_2} = 2.127$. For implementation within the FDTD method, auxiliary differential equation (ADE) finite-difference approximations were derived from the frequency dependent dielectric functions using the Z-transform method^{10,11}.

In addition to the structure, denoted the “coupled device” (CD), depicted in Fig. 7, several other auxiliary structures were simulated. In order to validate the models of the dispersive materials used in this work, thin films of Au and hBN in vacuo were simulated and the normal incidence absorptance, $A(\omega)$, spectrum for each of the films was calculated using $A(\omega) = 1 - [T(\omega) + R(\omega)]$, where $T(\omega)$ and $R(\omega)$ are the transmittance and reflectance spectra, respectively. These absorptance spectra were compared with the absorptance spectra calculated for the corresponding film using the transfer matrix

(TM) method¹² and excellent agreement between the two methods was observed.

Several other structures were simulated for comparison with the coupled device (CD): (i) The “bare device” (BD), this device is identical to the coupled device, but with the hBN layer removed. This device does not support phonon-polaritons. (ii) The “uncoupled device I” (UDCI), this device is identical to the coupled device, but with the hBN layer replaced with an equal thickness anisotropic layer that has $\epsilon_k(\infty)$ equal to the values for hBN, but the resonant behavior removed by setting $S_k = 0$. This device does not support phonon-polaritons. (iii) The “uncoupled device II” (UCDII), this device is identical to the coupled device, but with the nanopatterned Au layer replaced with an equal thickness layer of nanopatterned Si modelled by a frequency independent dielectric constant, $\epsilon_{Si} = 11.73$; this device does not support plasmons.

V. SOURCES

In order to perform useful stimulations an electromagnetic excitation needs to be introduced. Two common methods for this are discussed here: a pointwise hard source and a total field/scattered field (TFSF) source. For either source a time domain function is used to evolve the field value(s) at a specified location within the simulation space. While a harmonic source could be used this would fail to utilize the broadband frequency functionality of FDTD. For this reason much of the work in this dissertation was done using simulations excited by a Ricker wavelet [REF].

1. The Ricker Wavelet

$$\nu_r(t) = (1 - 2(\pi\nu_p(t - d_r)^2))e^{-(\pi\nu_p(t - d_r)^2)} \quad (6)$$

Where ν_p is the peak frequency and d_r is the temporal delay. The Ricker wavelet, (6), is a pulsed source equivalent to the second derivative of a Gaussian. The pulsing of the source enabled broad band simulations to be performed. Unlike a Gaussian pulse there is no dc component. The delay was able to be set such that the source “turned on” gradually. This gradual nature combined with a lack of a dc component reduced the occurrence of non-physical numerical artifacts in simulations. The spectral content was centered around a peak frequency in the spectral range of interest for each study.

A. Point Sources

A point source in FDTD is simulated by varying a single (or array of single) grid points using a source function of the form discussed in the previous section. These

sources are useful for simulating dipoles or artificial point sources, such as an afm tip.

B. TFSF Source

A Total Field Scatter Field (TFSF) source allows the simulation of a “one-way” plane wave. By subtracting the backwards propagating portion of the source from the grid point half a cell dimension “behind” the source a space in the simulation is created where only non-negligible electric or magnetic field strength is due to signal which has been reflected, or scattered, from an object in the simulation. This is particularly useful when it comes to calculating reflection spectra.

VI. BOUNDARY CONDITIONS

In order to simulate realistic structures it was necessary to incorporate boundaries into our simulation. For periodic structures their properties were ascertained by utilizing *periodic* boundaries. Where a photonic band structure was the desired output these boundaries were varied to become Bloch periodic boundaries. In the case of a terminal boundary, such as an “infinite” substrate or incident medium, an absorbing boundary was used called a Perfectly Matched Layer (PML).

A. PEC Boundary

B. Periodic Boundary

To simulate an infinite sheet of meta materials the most basic unit cell was repeated ‘infinitely’. This was accomplished by bounding the simulation in the x - and y -direction with a periodic boundary. This is accomplished by updating the discretized curl equation along the upper boundary (lower boundary for the magnetic field curl equation) explicitly. An example can be seen in (7)

$$E_y^t(x, 0, z) - E_y^t(x, N_y, z) \quad (7)$$

Where N_y is the size of the simulation space in the y -direction. When the cells at $y = N_y$ are updated the term $E_y^t(x, y+1, z)$ is replaced with $E_y^t(x, 0, z)$. Thus any signal exiting through a cell along the $y = N_y$ boundary reenters the simulation at $y = 0$. To create an infinite two dimensional simulation space this procedure is repeated along the x axis as well.

1. Bloch Periodic Boundary

C. Perfectly Matched Layers

D. UPML

E. CPML

VII. MATERIALS MODELS

A. Isotropy

1. Isotropic

2. Anisotropic

3. Diagonally Anisotropic

B. Dielectric Materials

C. Dispersive materials

1. Z Transform

2. Drude Model

3. Debye Drude Model

4. Lorentz

5. Diagonally Anisotropic

VIII. SENSORS

A. Time domain sensors

B. Frequency Domain Sensors

1. Heat Maps

2. RTA Spectra

IX. ANALYSIS TOOLS

A. Types

1. Spectral

2. Photonic Band

3. Dispersion

4. Heat Map

B. Imaging

C. Raster Dispersion

An investigation of the coupling of phonon-polaritons with plasmon-polaritons in hBN/nanopatterned Au layered devices

XI. INTRODUCTION

The details of the principle nanopatterned structure simulated in this chapter are shown in Fig. 7. The structure was composed of an 80 nm sheet of hexagonal boron nitride (hBN) deposited on a 50 nm thick film of nanopatterned Au atop of a SiO₂ substrate. The Au film was patterned with cross-shaped apertures. The aperture dimensions were $l = 0.8 d_{CC}$ and $w = 0.15 d_{CC}$, where d_{CC} was the model periodicity in the congruent x - and y -dimensions, which was varied during this work.

XII. RESULTS AND DISCUSSION

A. Far-Field Analysis

In order to investigate the effect of tuning the plasmon resonance through the hBN restrahlen band, a series of FDTD simulations were performed at a range of distances between the nearest neighbor centers of the crosses, (*i.e.*, d_{CC} in the range 2.34 – 3.94 μm) and the absorptance spectra for the bare device (BD), the uncoupled device I (UCDI) and the coupled device (CD) structures were calculated from the frequency resolved Poynting vector data collected by the planar DFT sensors described in Section (insert reference). Fig. 8 shows the absorption spectra calculated for all three devices. As can be seen clearly in Fig. 8 (a) and (b), for both the BD and UCDI, a red shift in the absorptance spectrum was observed as the value of d_{CC} was increased. Thus the absorptance feature due the plasmon resonance can be tuned with respect to the hBN restrahlen band and the coupling between plasmons in the nanostructured Au layer and phonon polaritons in the hBN layer investigated. As can be seen by comparing the spectra in Fig. 8 (a) and (b), the absorption spectrum of the UCDI is slightly red shifted compared with that of the BD for a given d_{CC} . The vertical dashed lines in Fig. 8 indicate the positions of the hBN TO and LO phonons at 1360 and 1614 cm^{-1} , respectively. The absorption spectrum of an 80 nm thick free-standing hBN film (Reference) is resonant with the TO phonon frequency. As can be seen from Fig. 8 (b), the UCDI structure with $d_{CC} = 3.14 \mu\text{m}$ exhibits a plasmon absorptance peak that is most closely resonant with the hBN TO phonon and this device is the one studied most extensively in this chapter.

Fig. 8 (c) shows the absorption spectra for a series of CDs for a range of d_{CC} . Also shown in Fig. 8 (c) is the absorptance spectrum of the UCDII with $d_{CC} = 3.14 \mu\text{m}$ (gray dotted line), which exhibits a single peak centered close to the hBN TO frequency. The most prominent

X. OTHER METHODS

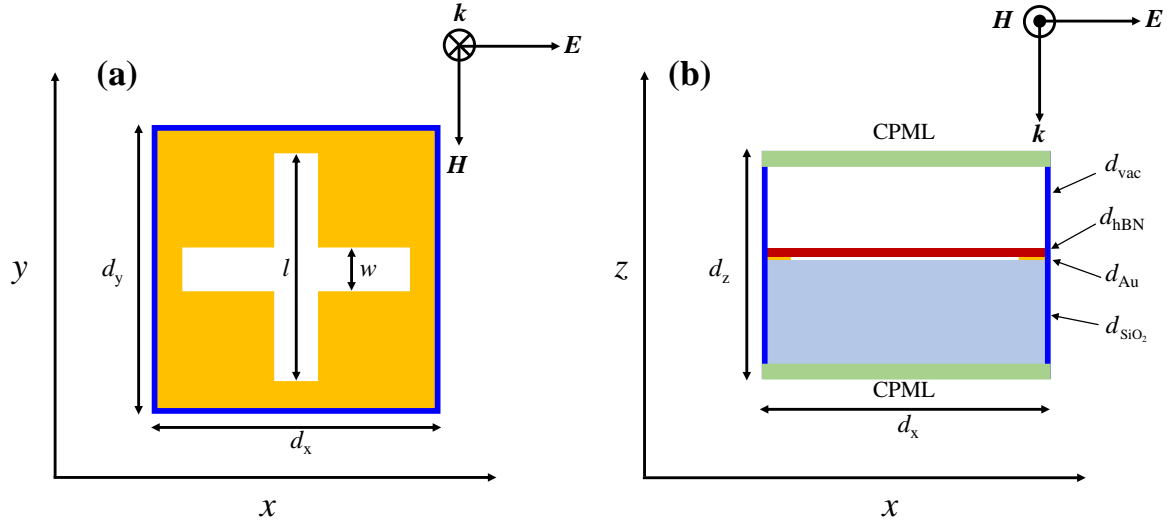


FIG. 2: (Color online) Schematic of the hBN/Au structure simulated in this work. (a) Planar view at the hBN/Au interface. (b) Cross-sectional view. CPML: Convolutional perfectly matched layer boundary conditions are imposed at the z -direction boundaries. Periodic boundary conditions are imposed at the x and y boundaries. The unit cell lengths in the x - and y -directions are d_x and d_y , respectively. The layer thicknesses are $d_{\text{vac}} = 0.87 \mu\text{m}$, $d_{\text{hBN}} = 80 \text{ nm}$, $d_{\text{SiO}_2} = 1.0 \mu\text{m}$, $d_{\text{Au}} = 50 \text{ nm}$. The length of the long segments of the cross pattern is $l = 0.8 d_x = 0.8 d_y$ while the width of the cross is $w = 0.15 d_x = 0.15 d_y$. The distance between the centers of neighboring crosses is $d_{\text{CC}} = d_x = d_y$. The directions of the \mathbf{E} -field, \mathbf{H} -Field and propagation vector \mathbf{k} are shown in both panes.

effect observed in the CD is that the plasmon absorption spectra in UCDI split into two main peaks either side of the hBN TO phonon frequency, with the peaks for $d_{\text{CC}} = 3.14 \mu\text{m}$ device being shifted approximately equal amounts above and below the hBN TO phonon frequency.

Another notable feature that is observed in most of the absorptance spectra depicted in Fig. 8 (c), is a small peak centered close to the hBN TO phonon frequency, which is also close to the center of the absorptance peak of the non-plasmonic UCDII. Less obvious in these spectra, but also present are a series of small peaks and shoulders that lie between the hBN TO and LO frequencies, the nature of these latter features will be elucidated below.

Finally, there are a series of cusps that occur in the spectra of all three devices, only one of which is shown in Fig. 8. This feature occurs at a frequency of $\sim 1750 \text{ cm}^{-1}$ for all three $d_{\text{CC}} = 3.94 \mu\text{m}$ devices. The assignment of these latter features will be deferred until later in this chapter.

In order to better analyze the absorptance peak frequency shifts observed in Fig. 8, the data in Fig. 8(b) and (c) were plotted in colormap form as a function of ν_{bare} as prescribed in Wan *et al.*¹³ in Fig. 9(a) and 9 (b) respectively. These plots can act as a proxy for the dis-

persion curves, although with some limitations. The peak positions in the absorptance spectra were determined using a simple peak fitting algorithm¹⁴ and plotted on top of the colormaps. In both Fig. 9 (a) and (b), the peaks in the spectra indicated by the orange, green and blue triangles are due to Rayleigh anomalies^{15–17} with indices (0,1), (1,1), (0,2), and their symmetric counterparts, respectively. The red squares in Fig. 9(a) indicate the main absorptance peak due to the plasmon-polariton in the UCDI. These peaks track linearly with ν_{bare} , the peak of the absorptance of corresponding BD and is analogous to the reflection data presented by Wan *et al.*¹³ in their Fig. 3(a). The red squares in Fig. 9(b) show how the absorptance peak due to the plasmon-polariton in UCDI splits due to the interaction with the bulk phonon-polariton in the hBN. The circles in Fig. 9(b) are interpreted as indicating slab phonon-polariton modes in the hBN layer; this interpretation will be further supported by the near-field data below.

B. Near-Field Analysis

In order to gain insight into the coupling between the plasmon-polaritons in the nanopatterned Au and the

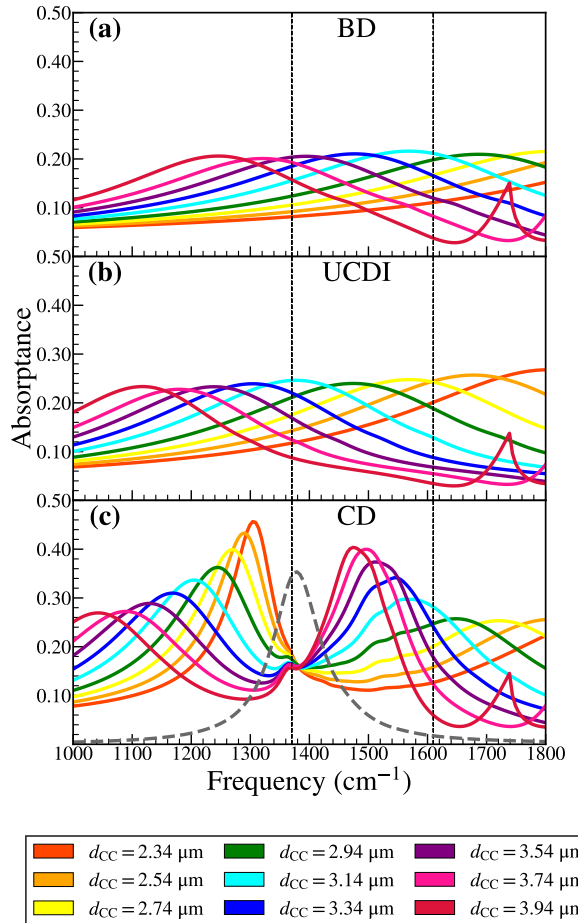


FIG. 3: (Color online) (a) The absorptance spectrum of the BD for a range of d_{CC} values. (b) The absorptance spectra of the UCDI. (c) The absorptance spectra of the CD. The gray dotted curve in pane (c) depicts the absorption spectra for the UCDII with $d_{\text{CC}} = 3.14 \mu\text{m}$. The vertical black dashed lines in this figure indicate the position of the hBN TO and LO phonon frequencies as described in the main text.

phonon-polaritons in hBN film, the electric field distributions, $|\mathbf{E}|$, at the position of the vacuum/hBN interface were investigated for all four devices, *i.e.*, BD, UCDI, UCDII, and CD, as shown in Fig. 10. This position was selected as these field distributions are accessible to experimental techniques. In order to gain additional insight, the cross-sectional field maps (which are not accessible experimentally) are also shown in Fig. 10 directly below the corresponding planar data. Fig. 10 presents data after y -polarized excitation at three different frequencies, *i.e.*, below the hBN restrahlen band at $\nu = 1200 \text{ cm}^{-1}$, within the hBN restrahlen band at $\nu = 1500 \text{ cm}^{-1}$ and above the restrahlen band at $\nu = 1700 \text{ cm}^{-1}$. The data excited at frequencies above and below the restrahlen band is expected to be predominantly plasmonic in nature for BD, UCDI and CD; this

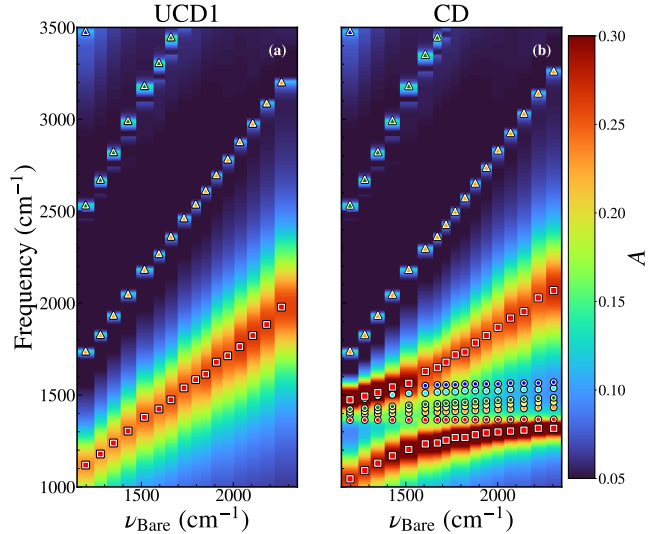


FIG. 4: (Color online) (a) Absorptance spectra for the UCDI vs the peak frequency of the BD (ν_{bare}) plotted as a color map. The symbols indicate the peaks in the absorptance spectra. The triangular symbols are due to Rayleigh anomalies, while the square symbols indicate the plasmon-polariton, which shifts linearly with ν_{bare} . (b) Absorptance spectra for the CD vs the peak frequency of the BD (ν_{bare}) plotted as a color map. The symbols indicate the peaks/shoulders in the absorptance spectra. The triangular symbols are due to Rayleigh anomalies, while the square symbols show the interaction between plasmon-polariton in the nanopatterned Au film and the bulk phonon-polariton in the hBN. The interpretation of the features labeled by the circular symbols are given in the main text.

is borne out by the data in Fig. 10 (a)–(h) and (q) – (x), respectively. In particular, in the case of the BD, there are field hot-spots at the inner corners of the cross pattern. In both the UCDI and CD, these hot spots are reproduced and smeared out; in the case of the CD this is due the presence of the hBN capping layer. The UCDII exhibits no evidence of field hot-spot behavior as expected for a structure without a nanostructured metallic layer. It is noticeable that in all the above cases the only rapid variations in the field take place right at the boundary between the metal/dielectric cross and the enclosed vacuum. Based upon the above discussion, the field maps shown in panes (b) and (r) of Fig. 10 are taken to be a prototypical signature of plasmonic behavior in the capped devices considered in this paper. In the case of the CD, see Fig. 10 (d) and (t), the field maps are very similar to those depicted in Fig. 10 (b) and (r), indicating that the behavior observed is predominately plasmonic when this device is excited either above or below the hBN restrahlen band.

Excitation of the above devices within the hBN restrahlen band at $\nu = 1500 \text{ cm}^{-1}$ reveals significantly different behavior. In the case of the BD and UCDI, the planar, Fig. 10 (i) and (j), and cross-sectional field maps, Fig. 10 (m) and (n), strongly resemble the plasmonic field maps excited outside the restrahlen band, in particular those excited at $\nu = 1700 \text{ cm}^{-1}$. The UCDII planar field map, Fig. 10 (k), exhibited high spatial frequency variations in the y -direction in the region within the cross, although there is comparatively little high spatial frequency variation in the x -direction. This behavior is reproduced outside the cross, but at a noticeably different spatial frequency. An examination of the cross-sectional field map, Fig. 10 (o), reveals that there is a guided slab mode within the hBN layer of this device. The CD planar field map, Fig. 10 (l), exhibited high spatial frequency variations in both the x - and y -directions in the regions within and outside the cross. The contrast of these spatial variations is somewhat greater than that observed in Fig. 10 (k). An examination of the cross-sectional field map, Fig. 10 (p), also shows strong evidence of a guided mode within the hBN layer of this device. The high spatial frequency variation observed in the planar field maps and the guided mode behavior observed in the cross-sectional field maps is taken to be a prototypical signature of polaritonic behavior in the devices considered in this paper.

Two notable differences between the behavior of UCDII and the CD are as follows: (i) the contrast in the spatial field variation is a factor of $\sim 2 - 3$ times higher in the CD than the UCDII suggesting that the plasmon plays a role in coupling energy into the hBN phonon-polaritons. (ii) the spatial variation of the field in the x -direction in the CD, which is not present in the UCDII device, indicate that the plasmon also plays a key role in launching phonon-polaritons into different directions within the hBN layer.

For potential comparison to experiment, it is useful to analyze lineouts from field data of the type presented in Fig. 10. A series of lineouts for a CD with $d_{\text{CC}} = 3.14 \mu\text{m}$ is shown in Fig. 11 (a). The electric fields were frequency resolved in the range $\nu = 1490 - 1570 \text{ cm}^{-1}$. The position of the lineout is indicated by the white line in the insert of Fig. 11 (b). Lineout data was only extracted outside of the cross region, *i.e.*, where the hBN was supported by an Au layer. The peaks in $|\mathbf{E}|$ were determined using the peak fitting algorithm described above. A phonon-polariton wavelength was assigned by calculating the averages of the differences between successive peaks. These wavelengths were found to lie in the range $140 - 330 \text{ nm}$. These data were used to construct a dispersion curve as shown in Fig. 11 (b). Additional insight can be obtained by examining the individual field components¹⁸, thus a similar process was applied to the E_y lineout data as shown in Fig. 11 (c) and (d). As can be seen by comparing the plots in Fig. 11 (b) and (d), the computed dispersion curves are similar although not identical, particularly at low values of q .

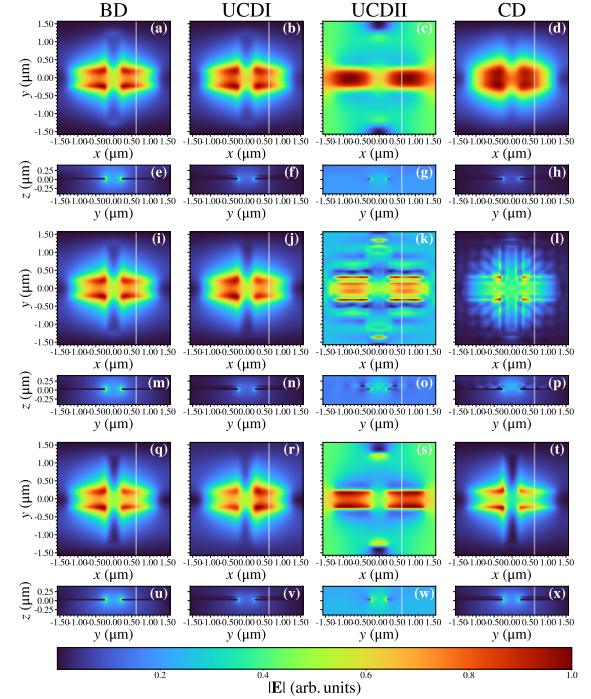


FIG. 5: (Color online) Background subtracted and normalized planar and cross-sectional colormaps of the field magnitude for the BD, UCDI, UCDII, and CD with $d_{\text{CC}} = 3.14 \mu\text{m}$. Panes (a) – (h) were excited below the restrahlen band at $\nu = 1200 \text{ cm}^{-1}$. The white lines in the planar colormaps panes (a) – (d) indicate the location of the cross-sectional colormaps in (e) – (h). Panes (i) – (p) were excited in the restrahlen band at $\nu = 1500 \text{ cm}^{-1}$. The white lines in the planar colormaps panes (i) – (l) indicate the location of the cross-sectional colormaps in (m) – (p). Panes (q) – (x) were excited above the restrahlen band at $\nu = 1700 \text{ cm}^{-1}$. The white lines in the planar colormaps panes (q) – (t) indicate the location of the cross-sectional colormaps in (u) – (x).

Fig. 12 (a) reproduces the far-field absorption spectrum from Fig. 8 (c) for convenient comparison with the near field data. Fig. 12 (b) shows E_y lineouts in the y -direction for frequencies in the range $\nu = 1000 - 1800 \text{ cm}^{-1}$ at intervals of 1 cm^{-1} . As can be seen from this figure, the region of highest field strength is in the vicinity of the inner Au–vacuum boundary within the cross (vacuum below the hBN layer), however features can be clearly resolved outside the cross (gold below the hBN layer). Broad features attributed to plasmons can be observed both below and above the restrahlen band; these features extend from inside the vacuum region into the gold region. Within the frequency range spanned by the restrahlen band, multiple branches can be observed in both the vacuum and Au regions.

Fig. 12 (c) shows the spatial Fourier transform of the (full spatial lineout) data described above. The resulting plot of $|E_y(q, \omega)|$ enables the phonon-polariton dispersion

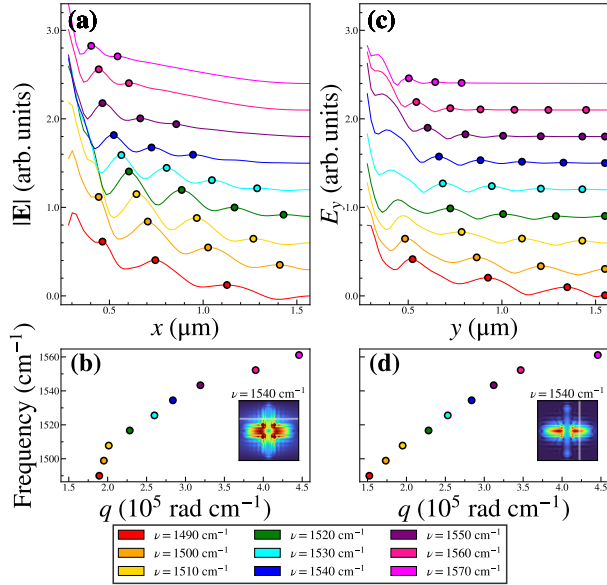


FIG. 6: (Color online) (a) Lineouts of the magnitude of the electric field for a range of excitation frequencies in the restrahlen band $\nu = 1490 - 1570 \text{ cm}^{-1}$. The circular dots indicate peaks in the lineout. (b) Dispersion curve constructed from the peak data in pane (a). (c) Lineouts of the y -component of the electric field for a range of excitation frequencies in the restrahlen band $\nu = 1490 - 1570 \text{ cm}^{-1}$. The circular dots indicate peaks in the lineout. (d) Dispersion curve constructed from the peak data in pane (c). The inserts in panes (b) and (d) show the position of the lineouts in panes (a) and (c).

curves to be visualized. In order to aid the interpretation of the data in Fig. 12 (c), theoretical phonon-polariton dispersion curves were calculated for a pair of three-layer thin-film structures: (i) Vacuum/hBN/Vacuum, and (ii) Vacuum/hBN/Au. The dispersion curves were calculated by finding the maxima of the imaginary part of the complex Fresnel reflection coefficient at real momenta as described in detail in the supplemental materials of the 2014 paper by Dai *et al.*¹⁹. The curves in green are for the Vacuum/hBN/Vacuum structure, while the curves in red are for the Vacuum/hBN/Au structure. The dispersion curves calculated in this manner were in good agreement (in their region of overlapping validity, *i.e.*, at high wavevector) with the dispersion curves calculated using the quasistatic approximation^{7,19},

$$q(\omega) = -\frac{\Psi}{d_{\text{hBN}}} \left[\tan^{-1} \left\{ \frac{\varepsilon_0}{\varepsilon_{x,y}(\omega)\Psi} \right\} + \tan^{-1} \left\{ \frac{\varepsilon_s}{\varepsilon_{x,y}(\omega)\Psi} \right\} + n\pi \right], \quad (8)$$

where $\Psi = -i\sqrt{\varepsilon_z(\omega)/\varepsilon_{x,y}(\omega)}$ and $\varepsilon_{x,y,z}(\omega)$ are the components of the hBN dielectric tensor, $\varepsilon_{\text{hBN}}(\omega)$.

$\varepsilon_s = \varepsilon_0$, the permittivity of free space for the Vacuum/hBN/Vacuum structure and $\varepsilon_s = \varepsilon_{\text{Au}}(\omega)$ for the Vacuum/hBN/Au structure; n is an integer and all other quantities are defined above. The advantage of Eq. 8 is that it explicitly highlights that the phonon-polariton dispersion clearly has multiple branches, and that those branches are labelled by n .

- [1] Joshua D. Caldwell, Andrey V. Kretinin, Yiguo Chen, Vincenzo Giannini, Michael M. Fogler, Yan Francescato, Chase T. Ellis, Joseph G. Tischler, Colin R. Woods, Alexander J. Giles, Minghui Hong, Kenji Watanabe, Takashi Taniguchi, Stefan A. Maier, and Kostya S. Novoselov. Sub-diffractive volume-confined polaritons in the natural hyperbolic material hexagonal boron nitride. *Nat. Commun.*, 5(1):5221, 2014.
- [2] Norman Ricker. Further developments in the wavelet theory of seismogram structure. *Bulletin of the Seismological Society of America*, 33(3):197–228, 1943.
- [3] DE Merewether, R Fisher, and FW Smith. On implementing a numeric huygen's source scheme in a finite difference program to illuminate scattering bodies. *IEEE Trans. Nucl. Sci.*, 27(6):1829–1833, 1980.
- [4] Branko D Gvozdic and Dusan Z Djurdjevic. Performance advantages of cpml over upml absorbing boundary conditions in fdtd algorithm. *J. Electr. Eng.*, 68(1):47–53, 2017.
- [5] Zachary S Sacks, David M Kingsland, Robert Lee, and Jin Fa Lee. A perfectly matched anisotropic absorber for use as an absorbing boundary condition. *IEEE Trans. Antennas Propag.*, 43(12):1460–1463, 1995.
- [6] Raymond C. Rumpf. Formulation of Plane Wave Expansion Method, EMPossible, 2020. [Online; accessed 7-July-2021].
- [7] Anshuman Kumar, Tony Low, Kin Hung Fung, Phaedon Avouris, and Nicholas X. Fang. Tunable lightmatter interaction and the role of hyperbolicity in graphenehbn system. *Nano. Lett.*, 15(5):3172–3180, 2015.
- [8] Yuyu Jiang, Xiao Lin, Tony Low, Baile Zhang, and Hongsheng Chen. Group-velocity-controlled and gate-tunable directional excitation of polaritons in graphene-boron nitride heterostructures. *Laser Photonics Rev.*, 12(5):1800049, 2018.
- [9] Arkadiusz Ciesielski, Lukasz Skowronski, Marek Trzcinski, Ewa Grecka, Pawe Trautman, and Tomasz Szoplik. Evidence of germanium segregation in gold thin films. *Surf. Sci.*, 674:73–78, 2018.
- [10] Dennis M. Sullivan. Z-transform theory and the fdtd method. *IEEE Trans. Antennas Propag.*, 44(1):28–34, 1996.
- [11] Dennis M. Sullivan. *Electromagnetic Simulation Using the FDTD Method, Second Edition*. Wiley, 2013.
- [12] H.A. MacLeod. *Thin-Film Optical Filters*. CRC Press, 2001.
- [13] Weiwei Wan, Xiaodong Yang, and Jie Gao. Strong coupling between mid-infrared localized plasmons and phonons. *Opt. Express*, 24(11):12367–12374, May 2016.
- [14] Peak positions were initially found using a naive peak finding algorithm that sequentially determined all local maxima. This procedure was validated by comparing to a fit to multiple Gaussian functions, although the latter approach would fail in regions where multiple peaks and shoulders were close in frequency. In the case of the inflections in the vicinity of the TO frequency side peaks or shoulders were determined by calculating the second derivative of the spectrum; the resulting curve was then multiplied by -1 and the above peak finding algorithm reapplied.
- [15] R. W. Wood. On a remarkable case of uneven distribution of light in a diffraction grating spectrum. *Lond. Edinb. Dublin Philos. Mag. J. Sci.*, 4:396402, 1902.
- [16] L. Rayleigh. On the dynamical theory of gratings. *Proc. R. Soc. Lond. A.*, 79:399416, 1907.
- [17] H. Gao, J. M. McMahon, M. H. Lee, J. Henzie, S. K. Gray, G. C. Schatz, and T. W. Odom. Rayleigh anomaly-surface plasmon

- polariton resonances in palladium and gold subwavelength hole arrays. *Opt. Express*, 17:23342340, 2009.
- [18] Angela E. Klein, Norik Janunts, Michael Steinert, Andreas Tünnermann, and Thomas Pertsch. Polarization-resolved near-field mapping of plasmonic aperture emission by a dual-snom system. *Nano. Lett.*, 14:50105015, 2014.
- [19] S Dai, Z Fei, Q Ma, AS Rodin, M Wagner, AS McLeod, MK Liu, W Gannett, W Regan, and K Watanabe. Tunable phonon polaritons in atomically thin van der waals crystals of boron nitride. *Science*, 343(6175):1125–1129, 2014.
- [20] D.J.T Heneghan, W. M. Dennis, 2021, *Journal TBD*, Vol. TBD, No. TBD. Reprinted here with permission of publisher and authors.
- [21] KB Tolpygo. Physical properties of a rock salt lattice made up of deformable ions. *Zh. Eksp. Teor. Fiz.*, 20:497–509, 1950.
- [22] K. U. N. Huang. Lattice vibrations and optical waves in ionic crystals. *Nature*, 167(4254):779–780, 1951.
- [23] A. J. Huber, B. Deutsch, L. Novotny, and R. Hillenbrand. Focusing of surface phonon polaritons. *Appl. Phys. Lett.*, 92(20):203104, 2008.
- [24] William L. Barnes, Alain Dereux, and Thomas W. Ebbesen. Surface plasmon subwavelength optics. *Nature*, 424(6950):824–830, 2003.
- [25] R. H. Ritchie. Plasma losses by fast electrons in thin films. *Phys. Rev.*, 106(5):874–881, 1957.
- [26] David Pines and David Bohm. A collective description of electron interactions: II. collective vs individual particle aspects of the interactions. *Phys. Rev.*, 85(2):338–353, 1952.
- [27] John Pendry. Playing tricks with light. *Science*, 285(5434):1687–1688, 1999.
- [28] R. Estevam da Silva, R. Macdo, T. Dumelow, J. A. P. da Costa, S. B. Honorato, and A. P. Ayala. Far-infrared slab lensing and subwavelength imaging in crystal quartz. *Phys. Rev. B*, 86(15):155152, 2012.
- [29] Nicholas Fang, Hyesog Lee, Cheng Sun, and Xiang Zhang. Sub-diffraction-limited optical imaging with a silver superlens. *Science*, 308(5721):534–537, 2005.
- [30] Katrin Kneipp, Yang Wang, Harald Kneipp, Lev T Perelman, Irving Itzkan, Ramachandra R Dasari, and Michael S Feld. Single molecule detection using surface-enhanced raman scattering (sers). *Phys. Rev. Lett.*, 78(9):1667, 1997.
- [31] Chad E Talley, Joseph B Jackson, Chris Oubre, Nathaniel K Grady, Christopher W Hollars, Stephen M Lane, Thomas R Huser, Peter Nordlander, and Naomi J Halas. Surface-enhanced raman scattering from individual au nanoparticles and nanoparticle dimer substrates. *Nano. Lett.*, 5(8):1569–1574, 2005.
- [32] Daniel Rodrigo, Odeta Limaj, Davide Janner, Dordaneh Etezadi, F. Javier Garca de Abajo, Valerio Pruneri, and Hatice Altug. Mid-infrared plasmonic biosensing with graphene. *Science*, 349(6244):165–168, 2015.
- [33] Alireza Fali, Samuel T. White, Thomas G. Folland, Mingze He, Neda A. Aghamiri, Song Liu, James H. Edgar, Joshua D. Caldwell, Richard F. Haglund, and Yohannes Abate. Refractive index-based control of hyperbolic phonon-polariton propagation. *Nano. Lett.*, 19(11):7725–7734, 2019.
- [34] DE Chang, Anders Sndberg Srensen, PR Hemmer, and MD Lukin. Quantum optics with surface plasmons. *Phys. Rev. Lett.*, 97(5):053002, 2006.
- [35] A Gonzalez-Tudela, Diego Martin-Cano, Esteban Moreno, Luis Martin-Moreno, C Tejedor, and Francisco J Garcia-Vidal. Entanglement of two qubits mediated by one-dimensional plasmonic waveguides. *Phys. Rev. Lett.*, 106(2):020501, 2011.
- [36] Ganesh R Bhimanapati, Zhong Lin, Vincent Meunier, Yeon-woong Jung, Judy Cha, Saptarshi Das, Di Xiao, Youngwoo Son, Michael S Strano, and Valentino R Cooper. Recent advances in two-dimensional materials beyond graphene. *ACS Nano.*, 9(12):11509–11539, 2015.
- [37] Frank HL Koppens, Darrick E Chang, and F Javier Garcia de Abajo. Graphene plasmonics: a platform for strong lightmatter interactions. *Nano. Lett.*, 11(8):3370–3377, 2011.
- [38] S. A. Biehs, M. Tschikin, and P. Ben-Abdallah. Hyperbolic metamaterials as an analog of a blackbody in the near field. *Phys. Rev. Lett.*, 109(10):104301, 2012.
- [39] Yu Guo, Ward Newman, Cristian L Cortes, and Zubin Jacob. Applications of hyperbolic metamaterial substrates. *Adv. OptoElectron.*, 2012.
- [40] C. L. Cortes, W. Newman, S. Molesky, and Z. Jacob. Quantum nanophotonics using hyperbolic metamaterials. *J. Opt.*, 14(6):063001, 2012.
- [41] F. Bonaccorso, Z. Sun, T. Hasan, and A. C. Ferrari. Graphene photonics and optoelectronics. *Nat. Photon.*, 4(9):611–622, 2010.
- [42] Zubin Jacob, Igor I. Smolyaninov, and Evgenii E. Narimanov. Broadband purcell effect: Radiative decay engineering with metamaterials. *Appl. Phys. Lett.*, 100(18):181105, 2012.
- [43] Zhaowei Liu, Hyesog Lee, Yi Xiong, Cheng Sun, and Xiang Zhang. Far-field optical hyperlens magnifying sub-diffraction-limited objects. *Science*, 315(5819):1686–1686, 2007.
- [44] A. V. Kretinin, Y. Cao, J. S. Tu, G. L. Yu, R. Jalil, K. S. Novoselov, S. J. Haigh, A. Gholinia, A. Mishchenko, M. Lozada, T. Georgiou, C. R. Woods, F. Withers, P. Blake, G. Eda, A. Wirsig, C. Hucho, K. Watanabe, T. Taniguchi, A. K. Geim, and R. V. Gorbachev. Electronic properties of graphene encapsulated with different two-dimensional atomic crystals. *Nano. Lett.*, 14(6):3270–3276, 2014.
- [45] C. R. Dean, A. F. Young, I. Meric, C. Lee, L. Wang, S. Sorgenfrei, K. Watanabe, T. Taniguchi, P. Kim, K. L. Shepard, and J. Hone. Boron nitride substrates for high-quality graphene electronics. *Nat. Nanotechnol.*, 5(10):722–726, 2010.
- [46] C. R. Dean, L. Wang, P. Maher, C. Forsythe, F. Ghahari, Y. Gao, J. Katoch, M. Ishigami, P. Moon, M. Koshino, T. Taniguchi, K. Watanabe, K. L. Shepard, J. Hone, and P. Kim. Hofstadters butterfly and the fractal quantum hall effect in moiré superlattices. *Nature*, 497(7451):598–602, 2013.
- [47] B. Hunt, J. D. Sanchez-Yamagishi, A. F. Young, M. Yankowitz, B. J. LeRoy, K. Watanabe, T. Taniguchi, P. Moon, M. Koshino, P. Jarillo-Herrero, and R. C. Ashoori. Massive dirac fermions and hofstadter butterfly in a van der waals heterostructure. *Science*, 340(6139):1427–1430, 2013.
- [48] G. L. Yu, R. V. Gorbachev, J. S. Tu, A. V. Kretinin, Y. Cao, R. Jalil, F. Withers, L. A. Ponomarenko, B. A. Piot, M. Potemski, D. C. Elias, X. Chen, K. Watanabe, T. Taniguchi, I. V. Grigorieva, K. S. Novoselov, V. I. Falko, A. K. Geim, and A. Mishchenko. Hierarchy of hofstadter states and replica quantum hall ferromagnetism in graphene superlattices. *Nat. Phys.*, 10(7):525–529, 2014.
- [49] F. D. M. Haldane and S. Raghu. Possible realization of directional optical waveguides in photonic crystals with broken time-reversal symmetry. *Phys. Rev. Lett.*, 100(1):013904, 2008.
- [50] S. Raghu and F. D. M. Haldane. Analogs of quantum-hall-effect edge states in photonic crystals. *Phys. Rev. A*, 78(3):033834, 2008.
- [51] Guorui Chen, Aaron L. Sharpe, Patrick Gallagher, Ilan T. Rosen, Eli J. Fox, Lili Jiang, Bosai Lyu, Hongyuan Li, Kenji Watanabe, Takashi Taniguchi, Jeil Jung, Zhiwen Shi, David Goldhaber-Gordon, Yuanbo Zhang, and Feng Wang. Signatures of tunable superconductivity in a trilayer graphene moiré superlattice. *Nature*, 572(7768):215–219, 2019.
- [52] Guorui Chen, Aaron L. Sharpe, Eli J. Fox, Ya-Hui Zhang, Shaoxin Wang, Lili Jiang, Bosai Lyu, Hongyuan Li, Kenji Watanabe, Takashi Taniguchi, Zhiwen Shi, T. Senthil, David Goldhaber-Gordon, Yuanbo Zhang, and Feng Wang. Tunable correlated chern insulator and ferromagnetism in a moiré superlattice. *Nature*, 579(7797):56–61, 2020.
- [53] K. S. Novoselov, A. Mishchenko, A. Carvalho, and A. H. Castro Neto. 2d materials and van der waals heterostructures. *Science*, 353(6298):aac9439, 2016.
- [54] A. K. Geim and I. V. Grigorieva. Van der waals heterostructures. *Nature*, 499(7459):419–425, 2013.

- [55] Achim Woessner, Mark B. Lundeberg, Yuanda Gao, Alessandro Principi, Pablo Alonso-Gonzlez, Matteo Carrega, Kenji Watanabe, Takashi Taniguchi, Giovanni Vignale, Marco Polini, James Hone, Rainer Hillenbrand, and Frank H. L. Koppens. Highly confined low-loss plasmons in grapheneboron nitride heterostructures. *Nat. Mater.*, 14(4):421–425, 2015.
- [56] Bo Zhao and Zhuomin M. Zhang. Perfect mid-infrared absorption by hybrid phonon-plasmon polaritons in hbn/metal-grating anisotropic structures. *Int. J. Heat Mass Transf.*, 106:1025–1034, 2017.
- [57] Jiong Yang, Mohannad Mayyas, Jianbo Tang, Mohammad B. Ghasemian, Honghua Yang, Kenji Watanabe, Takashi Taniguchi, Qingdong Ou, Lu Hua Li, Qiaoliang Bao, and Kourosh Kalantar-Zadeh. Boundary-induced auxiliary features in scattering-type near-field fourier transform infrared spectroscopy. *ACS Nano*, 14(1):1123–1132, 2020.
- [58] F. J. Alfar-Mozaz, P. Alonso-Gonzlez, S. Vlez, I. Dolado, M. Autore, S. Mastel, F. Casanova, L. E. Hueso, P. Li, A. Y. Nikitin, and R. Hillenbrand. Nanoimaging of resonating hyperbolic polaritons in linear boron nitride antennas. *Nat. Commun.*, 8(1):15624, 2017.
- [59] Marta Autore, Peining Li, Irene Dolado, Francisco J. Alfar-Mozaz, Ruben Esteban, Ainhoa Atxabal, Flix Casanova, Luis E. Hueso, Pablo Alonso-Gonzlez, Javier Aizpurua, Alexey Y. Nikitin, Sal Vlez, and Rainer Hillenbrand. Boron nitride nanoresonators for phonon-enhanced molecular vibrational spectroscopy at the strong coupling limit. *Light Sci. Appl.*, 7(4):17172–17172, 2018.
- [60] T. G. Folland, A. Fali, S. T. White, J. R. Matson, S. Liu, N. A. Aghamiri, J. H. Edgar, R. F. Haglund, Y. Abate, and J. D. Caldwell. Reconfigurable infrared hyperbolic metasurfaces using phase change materials. *Nat. Commun.*, 9(1):4371, 2018.
- [61] Fei Cheng, Xiaodong Yang, and Jie Gao. Ultrasensitive detection and characterization of molecules with infrared plasmonic metamaterials. *Sci. Rep.*, 5(1):14327, 2015.
- [62] Yee Kane. Numerical solution of initial boundary value problems involving maxwell's equations in isotropic media. *IEEE Trans. Antennas Propag.*, 14(3):302–307, 1966.
- [63] A. Tafove and S.C. Hagness. *Computational Electrodynamics: The Finite-difference Time-domain Method*. Artech House, 2005.
- [64] PGI Compilers and Tools: OpenACC Getting Started Guide, NVIDIA, 11/19/2020 2020.
- [65] Edward D. Palik. *Handbook of optical constants of solids*. Academic Press, Orlando, 1985.
- [66] Jun John Sakurai and Jim Napolitano. *Modern Quantum Mechanics*. Cambridge University Press, 2017.
- [67] D.J.T Heneghan, W. M. Dennis, 2021, *Journal TBD*, Vol. TBD, No. TBD. Reprinted here with permission of publisher and authors.

[An Investigation of the Polariton-Plasmon Coupling in hBN on Nanopatterned Ag Layered Structures] An Investigation of the Polariton-Plasmon Coupling in hBN on Nanopatterned Ag Layered Structures²⁰

XIII. INTRODUCTION

Polaritons are quasiparticles resulting from hybrid modes of photons and charge dipole excitations in crystalline structures²¹. The two most common types of polaritons are phonon polaritons^{21–23} and surface plasmon polaritons²⁴, both of which are relevant to this study. First discovered by Ritchie in 1957²⁵, plasmon-polaritons were observed to propagate along surfaces of conducting thin films²⁶. These surface-plasmon-polaritons (SPPs) remain trapped on the surface due to resonant interactions with the free electrons of the conductor. A unique property of SPPs is that they couple to features within the crystal whose features are smaller than the free space wavelength of the initial coupling photon²⁷. This confinement of radiation to scales below the diffraction limit has become the primary focus of modern nanophotonics¹.

To develop scalable quantum-photonic technologies on-chip integration of the photonic components is required. Such devices have applications in subwavelength imaging^{28,29}, biosensing^{30–32}, thin film sensing³³ and quantum information^{34–36}. After its discovery much interest was shown in the study of graphene as a medium for tunable photon-plasmon coupling at the mid-infrared range³⁷. However, in the second decade of this century there has been a rapidly increasing number of papers in the study of non-graphene two dimensional materials³⁶. In 2014 Dai *et al.* demonstrated higher confinement within hexagonal boron nitride (hBN) with lower losses than graphene SPPs¹⁹ and a strong confinement regime up to $\lambda 861$ ¹. This advantageous property is due to the hyperbolic nature of hBNs permittivity tensor which contains oppositely signed principle components within the mid-infrared range⁷. While other artificial hyperbolic materials have been demonstrated, they suffer from higher losses and increased fabrication costs in comparison to natural hBN^{38–40}. Since hBN SPPs reside in a similar mid-infrared regime as graphenes, hBN has the potential to be used in similar devices to those fabricated using graphene such as solar panels⁴¹. While hBNs ability to endure temperatures up to 1773 K makes it a versatile material for high temperature applications^{42,43}. This shared absorptance range also allows for graphene-hBN hetero-devices^{44,45}. Proximity effects due to layered hBN-graphene interactions has been shown to lead to the formation of secondary Dirac points^{46–48}. Such properties are of use for breaking of time-reversal-symmetry^{49–51}, enabling the study of the quantum Hall effect^{46–48}, tunable superconductivity⁵¹, and topological currents and states^{52,53}. Graphenes high tunability to allows such devices to couple into a greater spectral range, while hBNs higher quality factor to transport SPPs at a higher efficiency with low levels of damping^{7,45,54,55}. However, the plasmon losses due to electron scattering by thermal phonons it is necessary to reduce dielectric losses by reducing damping⁵⁵.

One such solution for reducing this dielectric loss is to use a hetero device that incorporates a metallic diffrac-

tion grating underneath a hBN layer. Zhao and Zhang demonstrated near-perfect absorptance in hBN/metal gratings due to hyperbolic phonon-plasmon polariton coupling⁵⁶. Recently Yang *et al.*⁵⁷ reported the coupling of phonon-polaritons between a hexagonal pattern of circular cavities in SiO₂. The experimental observations in this work used a diffraction grating constructed of a hexagonal pattern of holes in an Ag film under an 80 nm thick layer of hBN and over a Si substrate. Up until recently it has been difficult to observe many of the finer near field spectral features of hBN devices due to lack of access to powerful broadband IR laser sources to effectively couple with optical phonons⁵⁷⁻⁵⁹. Recent work has shown scattering-type scanning near-field optical microscopy (s-SNOM) to be a powerful tool to observe, manipulate and quantify polariton coupling in hBN based heterostructures^{33,60}. Related studies investigating phonon-plasmon coupling using Fourier-transform infrared (FTIR) spectroscopy have been performed on polymethyl methacrylate (PMMA)^{13,61}. The results reported here involved a coupled experimental/simulative study of an hBN hetero device. The device is an hBN film atop of nanopatterned (hexagonal pattern of circular holes) silver (Ag) film deposited on a silicon (Si) substrate.

Computer simulations were performed using an in-house Finite-Difference Time-Domain (FDTD) code. FDTD is a technique for simulating electrodynamic systems by numerically integrating the Maxwell curl equations by using a finite-difference approximation. Initially proposed by Yee in 1966⁶² the popularity of the method has grown in parallel to the advances in computing over the last nine decades. The time-domain nature of FDTD means that several frequencies of interest can be studied from a single simulation by using a broadband source. FDTD gives us control over the parameter space to simulate a range of possible device specifications including grating pitch length, film thickness and hole size.

Due to the large time constants of the hBN and Ag films which comprised the devices studied in this investigation, $\geq 2 \times 10^6$ time steps time steps were needed for each simulation. This necessitated incorporating GPU acceleration into the inhouse code to greatly reduce the runtime required.

The FDTD simulations reported in this paper enable not only direct comparison with experimental s-SNOM images, but also can provide detailed three-dimensional spatial information on the vector components of the electric fields within the device, information on plasmon-polariton coupling and allow the polariton wavelength to be unambiguously extracted.

XIV. RESULTS AND DISCUSSION

Electromagnetic simulations were performed using the Finite-Difference Time-Domain (FDTD) method⁶² using an in-house designed code. The FDTD method numeri-

cally integrates the Maxwell curl equations with second-order accuracy as detailed in Ref.⁶³.

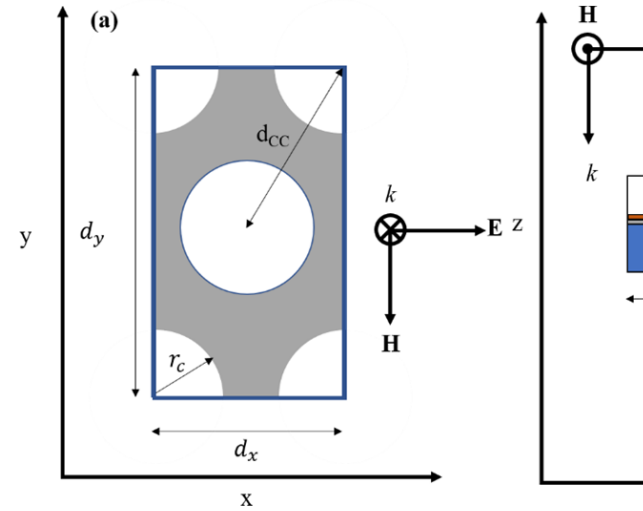


FIG. 7: Simulative structure.

Schematic of the hBN/Ag structure simulated on this work. (a) Plane view at the hBN/Ag interface. The symmetry reduced unit cell is outlined in red. (b) Cross-sectional view. CPML: Convolutional perfectly matched layer boundary conditions terminated the z direction boundaries. Periodic boundary conditions terminated the x and y boundaries. The unit cell lengths in the x- and y- directions are d_x and d_y , respectively. The layer thicknesses beyond the CPMLs were $d_{\text{VAC}} = 0.87 \mu\text{m}$, $d_{\text{hBN}} = 80 \text{ nm}$, $d_{\text{Si}} = 1.0 \mu\text{m}$, $d_{\text{Ag}} = 50 \text{ nm}$. The radius of the holes is $r_C = 0.68 \mu\text{m}$. The distance between the centers of the cylindrical holes is $d_{CC} = d_x$. The directions of the \mathbf{E} -field, \mathbf{H} -Field and propagation vector \mathbf{k} is shown in both panes.

The details of the nanopatterned structure simulated in this work are shown in Figure 7. The structure comprised of an 80 nm sheet of hexagonal boron nitride (hBN) deposited on a 50 nm thick film of nanopatterned Ag atop of a Si substrate. The Ag film was patterned with circular holes of radius 0.68 μm arranged in a hexagonal lattice with a distance between the centers of d_{CC} , which was varied during this work.

In order to decrease the runtime of the simulations GPU acceleration was used. A combination of OpenACC and CUDA⁶⁴ methodologies enabled the simulations to be sped up by a factor of 70. This enabled higher resolution simulations to be performed in the allowed time-frame.

For all simulations performed a broadband, plane wave source was used. The time profile of the source was a Ricker wavelet² centered on 1667 cm^{-1} ($6\mu\text{m}$). This source injects a laterally uniform in time pulse using the total-field scattered-field (TFSF) interface³. The source was x-polarized and propagated in the negative z-direction. The use of the TFSF method enabled sensors to be placed above the TFSF boundary in order to record only the reflected field values.

To prevent divergence in the simulation caused by the patterned Ag layer a convolutional perfectly matched layer (CPML)⁴ boundary was used as the CPML has been shown to be more stable than a uniaxial perfectly matching layer (UPML)⁵ absorbing boundary for simulations of this kind. Periodic boundary conditions are used in the transverse directions. In the positive and negative z-directions, the simulation was terminated by 50 perfectly matched layers. Due to the difference between the length scales of features in the transverse and longitudinal directions, the computational grid used cell sizes in the ratio of 10:10:1 in the x-, y- and z-dimensions, respectively. The resonance frequency of the patterned Ag layer was found to be sensitive to the spatial resolution used in the simulation, so convergence testing was performed, and a working resolution of $\Delta x = 20\text{ nm}$, $\Delta y = 20\text{ nm}$, $\Delta z = 2\text{ nm}$ was selected to be a good compromise between simulation accuracy and runtime.

Reflectance and transmittance spectra were calculated using a transverse wave vector expansion method from calculations performed by signal monitors during the simulation. Each of these monitors was a two-dimensional plane which calculated the discrete Fourier-transform (DFT) for the wavelengths of interest for every grid point within the monitors cross-sectional plane. The monitor performed this function for each of the three electric field components. The incidence data required to normalize the results were also calculated by DFT during the TFSF update step.

For direct comparison with the experimental imaging data, the spectrally resolved (using DFT) electric field as a function of position was exported from a sensor located on a plane at the hBN/vacuum interface. This data was visualized using a color map. The polariton wavelength could be extracted from the above data as discussed in this report and further detailed in the supplemental materials for direct comparison with experiment.

The various components of the device were modelled as follows. The Si substrate was simulated using a simple dielectric with $\varepsilon_r = 11.7$. The Ag film was simulated using wavelength dependent refractive index data as detailed in the Handbook of Optical Constants of Solids I-III⁶⁵ to fit to a Debye/Drude model. The hBN layer was simulated using a Lorentz model. i.e.,

$$\overleftrightarrow{\varepsilon} = \begin{pmatrix} \varepsilon_x & 0 & 0 \\ 0 & \varepsilon_y & 0 \\ 0 & 0 & \varepsilon_z \end{pmatrix}$$

where $\varepsilon_k(\infty)$ is the k th component (where $k=x,y,z$) of the dielectric function at infinity, ω_k is the frequency of a transverse optical phonon propagating in the k th direction, the factor $S_k\omega_k^2$ can be written in the form $\varepsilon_k(\infty)(\omega_{\text{LO}}^2 - \omega_{\text{TO}}^2)^7$, showing the explicit dependence on the longitudinal optical (LO) and transverse optical (TO) phonon frequencies. Given the polarization of the excitation source (see Figure 1) the in-plane parameters used in this research were $\varepsilon_{x,y}(\infty) = 4.87$, $S_{x,y} = 0.61$, $\hbar\omega_{x,y} = 170.1\text{ meV}$. The out-of-plane parameters were $\varepsilon_z(\infty) = 2.95$, $S_z = 0.61$, $\gamma_z = 0.25\text{ meV}$, and $\hbar\omega_z = 92.5\text{ meV}$ from ref.⁸. The notable exception was the planar damping constant $\gamma_{x,y}$, which has been shown to have a strong thickness dependence by Caldwell *et al.*¹. Using results from the Caldwell group, as detailed in the supplemental materials section, the appropriate value of $\gamma_{x,y}$ for a film thickness 83 nm was found to be 3.97 meV. For implementation in the FDTD method, finite-difference approximations were obtained by converting the respective frequency domain permittivity tensors to the time domain using the Z-transform method^{10,66}.

Figure 8 (a) and (b) shows the frequency dependence of the real and imaginary components of the dielectric tensor for an hBN film with a thickness of $dh\text{BN} = 80\text{ nm}$ suspended in vacuum. Figure 8 (c) shows the normal incidence reflectance, transmittance, and absorptance spectra for this film calculated using both the transfer matrix method and the FDTD method as detailed below. Frequency domain data was recorded in the FDTD simulations using the aforementioned DFT sensors. These sensors recorded the reflected and transmitted field data while a separate sensor within the TFSF source function recorded incident field data. This data was then used to calculate the ratio of reflected/transmitted and incident signal as a function of frequency. For the simulation in Figure 8 (c) these sensors were placed at $z = 0.01\text{ }\mu\text{m}$ and $z = 1.98\text{ }\mu\text{m}$. The absorptance (A) spectrum for the film was calculated using $A = 1 - (T + R)$ where the reflectance (R) and transmittance (T) spectra were calculated using DFT sensors.

In order to ensure resonance between the polaritons supported by the hBN layer and the plasmons supported by the nanopatterned Ag/Si structure (bare device). A series of FDTD simulations were performed at range of distances between the centers of the holes (d_{CC}). The absorptance spectrum for each of the structures was calculated as described above. As the value of d_{CC} was increased, a red shift in the absorptance spectrum was observed, as shown in Figure 9 (a). This observation enabled the absorptance resonance of the bare device to be tuned to close the resonance observed in Figure 8 (c) for an 80 nm thick layer of hBN. Following the ap-

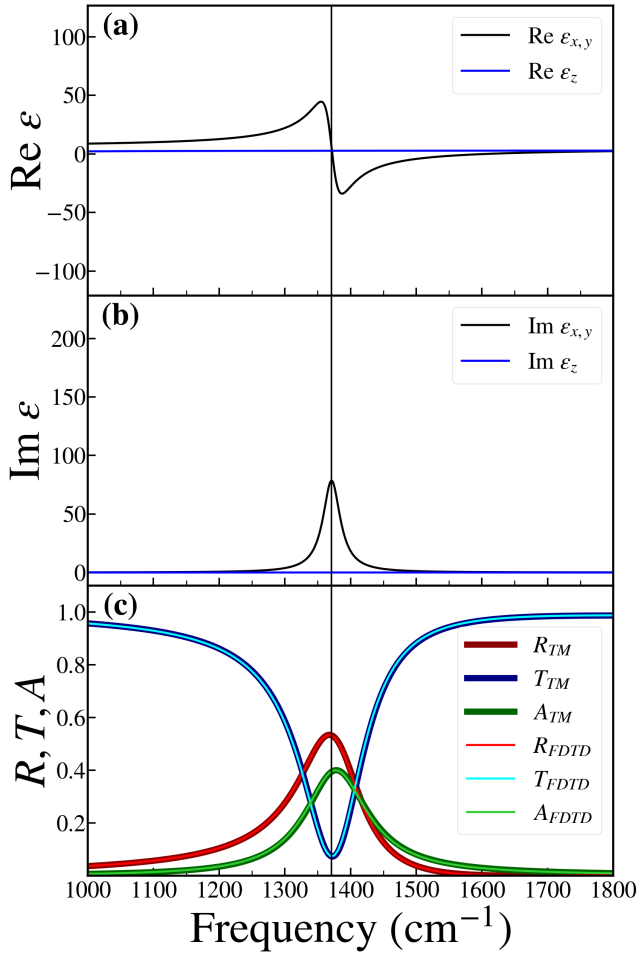


FIG. 8: Dielectric function and resulting spectra of 80 nm hBN.

(a) Real part of $\epsilon_{x,y}$ (black) and ϵ_z (blue) for hBN. (b) Imaginary part of $\epsilon_{x,y}$ (black) and ϵ_z (blue) for hBN. The vertical line in this figure indicates the peak of $\text{Im } \epsilon_{x,y}$ (c) Plot of reflectance (R), transmittance (T) and absorptance (A) for an 80 nm thin film of hBN in vacuum as calculated using both the transfer matrix and FDTD methods. The peak in absorptance occurs at 1377 cm^{-1} .

proach of Wan *et al.*¹³, the properties of a second series of devices (uncoupled devices) with a nonresonant dielectric layer on top of the nanopatterned Ag/Si structure (bare device) are also investigated. Specifically, for these devices, the top layer is an anisotropic dielectric with $\epsilon_{x,y}(\infty) = 4.87$ and $\epsilon_z(\infty) = 2.95$, respectively (i.e., $\epsilon_{x,y}(\infty)$ and $\epsilon_z(\infty)$ for hBN, respectively). The absorptance spectra for the uncoupled devices are shown

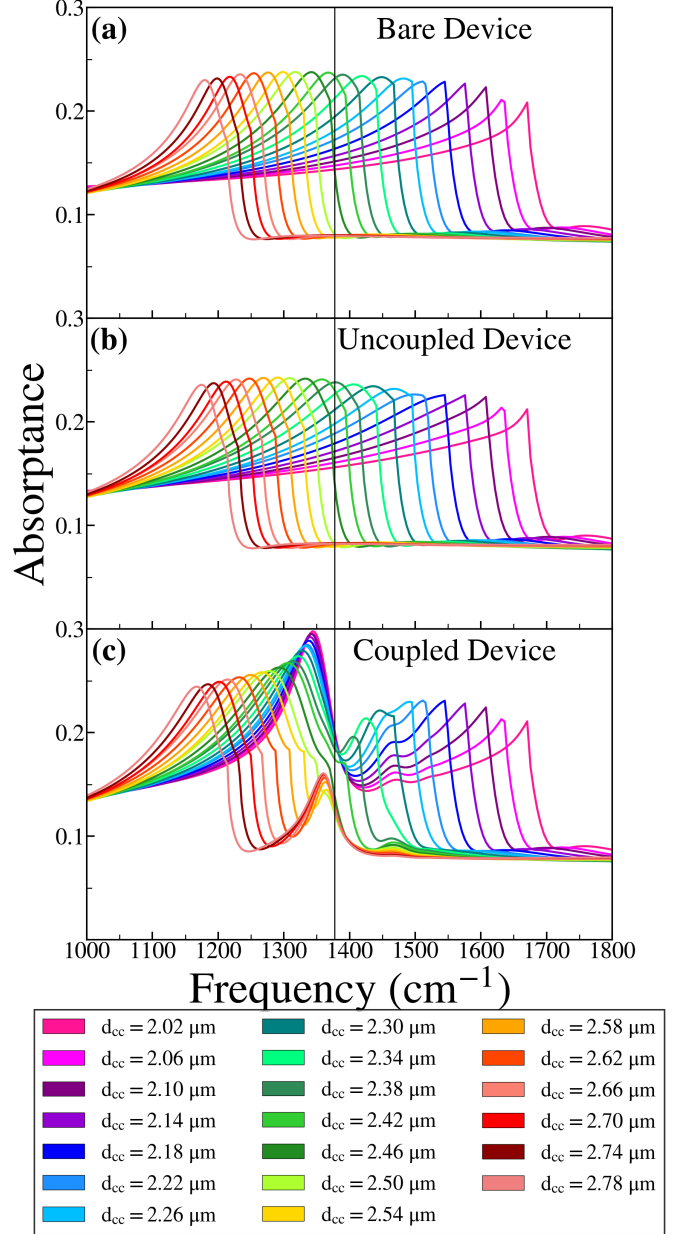


FIG. 9: Absorptance spectra for devices simulated.

(a) The absorptance spectrum of the bare nanopatterned Ag on Si device as function of d_{CC} . (b) The absorptance spectra of devices with an uncoupled anisotropic dielectric layer on top of the structures depicted in (a). (c) The absorptance spectra of devices with an hBN (coupled) layer on structures depicted in (a). The vertical black line in this figure indicates the absorption peak that was observed for the 80 nm thick layer of hBN in vacuum shown in Figure 8.

in Figure 9 (b). The peaks of the uncoupled device absorptance spectra are slightly red-shifted compared to the peaks of the bare device absorption spectra. The uncoupled device with an absorptance peak that is most

resonant with the hBN absorption peak is the device with $d_{CC} = 2.38 \mu\text{m}$. The final series of devices (coupled devices), comprising an 80 nm thick hBN layer on top of the bare devices. The absorptance of the coupled devices are shown in Figure 9 (c). In this case the absorptance spectra splits into two major peaks, the positions of which vary with d_{CC} or equivalently with the frequency (ν_{bare}) of the peak absorptance of the bare device. In addition, there is a smaller peak at 1468 cm^{-1} the position of which is independent of $d_{CC}(\nu_{\text{bare}})$, it is notable that this peak occurs in the spectral region where $\text{Re } \varepsilon_{x,y}$ is strongly negative.

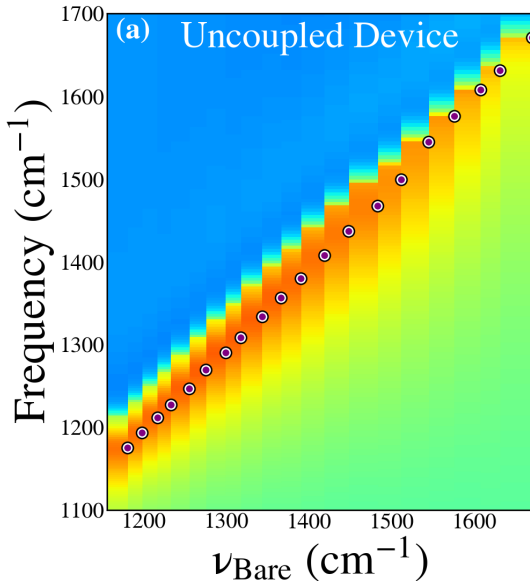


FIG. 10: Rasterized frequency "heat maps" for coupled and uncoupled devices

(a) Absorptance spectra for the uncoupled devices vs the peak frequency of the bare device. The symbols indicate the peak in the absorptance spectra of each uncoupled device and clearly show the tuning of the plasmon resonance as function of d_{CC} . (b) The absorptance spectra for the hBN (coupled) device. The symbols indicate the peaks in the absorptance spectra and clearly show the coupling between the plasmonic resonance and the hBN TO phonon mode.

In order to better analyze the absorptance peak frequency shifts observed in Figure 9, the data in Figure 9(b) and (c) were plotted in colormap form as a function of ν_{bare} in Figure 10(a) and 10 (b) respectively. The peak positions were calculated as detailed in the supplemental materials and plotted on top of the colormaps as prescribed in¹³. Analogously to the reflection data of Wan et al.¹³, the plasmon peak in the uncoupled device tracks linearly with ν_{bare} , while the absorptance peaks of the coupled device open up a small gap and splits into upper and lower branches. For the coupled device with

$d_{CC} = 2.38 \mu\text{m}$, the difference in frequency between the peaks in absorption is $\Omega = 89.7 \text{ cm}^{-1}$, which interestingly is close to the range of values, $\Omega = 63.4 - 86.7 \text{ cm}^{-1}$, reported by Wan et al. for the PMMA/gold meta material structures with PMMA thicknesses ranging from 40 - 100 μm . Application of degenerate perturbation theory⁶⁶ applied to this two-level system enabled the phonon-plasmon coupling strength $\Delta_{PP} = \Omega = 89.7 \text{ cm}^{-1}$ to be extracted.

Figure 11 shows components and magnitude of the electric field in a cross-section through center of both the coupled and uncoupled devices with $d_{CC} = 2.38 \mu\text{m}$. Data for devices with other values of d_{CC} are presented in the supplemental materials. The fieldmaps shown in Figure 11 are four of the frequencies of interest that were monitored within the hBN absorption peak in Figure 8(c), namely $\nu = 1299, 1361, 1471$, and 1538 cm^{-1} . By comparing the field maps of the coupled and uncoupled devices, it is possible to isolate the behavior associated with the hBN TO phonon mode. At $\nu = 1299 \text{ cm}^{-1}$ the field maps for both the coupled and uncoupled devices are very similar indicating that at this frequency the behavior of the coupled device is predominantly plasmonic. At $\nu = 1361 \text{ cm}^{-1}$, which is the lowest frequency point of upper branch in Figure 11 (b) and is close in frequency to the peak of the hBN in vacuum absorptance band in Figure 8 (c), the data in the coupled device appears to be predominantly plasmonic but the fields are confined in the region of the Ag and hBN layers. At $\nu = 1471 \text{ cm}^{-1}$, which is in the vicinity of the small fixed frequency absorptance peak in Figure 8 (c), field maps for both the coupled and uncoupled devices are very different indicating that at this frequency the behavior of the coupled device is predominantly due to the hBN TO phonon. It is notable that in this region the electric field is strongly confined to and appears to be guided within the hBN layer. Finally, at $\nu = 1538 \text{ cm}^{-1}$, the field maps for both the coupled and uncoupled devices are also very different indicating that at this frequency the behavior of the coupled device is predominantly due to the hBN TO phonon.

It is not immediately obvious how to extract the polariton wavelength (λ_P) from the above data, in particular the absolute value field data which is directly comparable to experiment. This is due in part not only to the variety and complexity of the mode structure but also due to a non-zero background contribution (see for example, the x-polarized data for the coupled devices in Figure 11). Fortunately, the y-polarized data is comparatively background free showing an alternating field pattern from which the phonon wavelength may be extracted. The y-polarized data was analyzed in the spectral region $1466 - 1570 \text{ cm}^{-1}$ and where possible, the distance between successive peaks was averaged (as described in the supplemental materials) in two regions: (a) In the region where the hBN layer was supported by Ag (denoted Vacuum—hBN—Ag) and (b) where the hBN was over one of the circular holes in the Ag film (denoted

Vacuum—hBN—Vacuum). In the Vacuum—hBN—Ag case phonon wavelengths in the range $\lambda_P = 0.16\text{--}0.33\text{ }\mu\text{m}$ were extracted. In the Vacuum—hBN—Vacuum case phonon wavelengths in the range $\lambda_P = 0.40\text{--}0.70\text{ }\mu\text{m}$ were extracted. The above values of λ_P were compared with phonon-polariton dispersion curves calculated using formalism described in [20] for (a) an 80 nm layer of hBN in the Vacuum—hBN—Ag configuration and (b) the Vacuum—hBN—Vacuum configuration. The phonon-polariton wavelengths calculated above were both found to lie close to the expected dispersion curves for the cases (a) and (b) above. There was one notable exception to the data described above. The value of $\lambda_P = 0.28\text{ }\mu\text{m}$ for the Vacuum—hBN—Vacuum case monitored at frequencies in the vicinity of $\nu = 1466\text{ cm}^{-1}$ was much shorter than expected value of $2.1\text{ }\mu\text{m}$ indicating that the field variation observed in this case is not solely due to the phonon-polariton, but is caused by some other effect, possibly strong confinement and guiding in the hBN layer.

Figure 12 presents a comparison of s-SNOM data and FDTD electric field (\mathbf{E}) data detected at the hBN/vacuum interface. In an examination of the s-SNOM data and the FDTD field map at 1389 cm^{-1} , both show a bright central spot. At 1408 cm^{-1} data show a sharp ring feature within the Ag hole. At 1449 cm^{-1} the ring feature moves further out towards the edge of the Ag hole. At 1538 cm^{-1} , there is a slow variation within the Ag hole with a weaker maximum at the center, while outside the Ag hole fine fringes can be observed which are attributed to phonon-polaritons. Finally, at 1562 cm^{-1} , the fringes inside the Ag hole move further toward the edge of the. Outside the Ag hole fine fringes can still be observed, although they are weaker than those observed in the 1538 cm^{-1} case. The above behavior can also be observed by comparing the line-out data in Figure 12 (k) and (l).

XV. CONCLUSION

The excitations that occur on a hBN/nanopatterned Ag device have been investigated using a combination of experimental (s-SNOM) and simulational (FDTD) techniques. The s-SNOM data shows high spatial frequency features when the structure is excited in the region $1370\text{--}1590\text{ cm}^{-1}$ and predominantly low spatial frequency features when excited outside of the spectral region. FDTD simulations of a model structure exhibit similar behavior. In addition, an examination of absorption spectra for the device indicates that the degenerate phonon and plasmon peaks split and shift enabling the phonon-plasmon coupling strength to be estimated, *i.e.*, $\Delta\text{PP} = 89.7\text{ cm}^{-1}$ to be made. Access to the individual field component afforded by the FDTD simulations enabled the polariton wavelength as function of frequency to be extracted. The results presented in this paper therefore contribute to a deeper and more fundamental understanding of the

interactions between phonons and plasmons in this and related structures and devices.

[Other Paper] Other Chapter⁶⁷

XVI. A YET TO BE SUBMITTED PAPER

XVII. STANDARD SECTION

This is a standard section

Conclusions Clearly your dissertation conclusions go here.

Extra Parameters

- [1]Joshua D. Caldwell, Andrey V. Kretinin, Yiguo Chen, Vincenzo Giannini, Michael M. Fogler, Yan Francescato, Chase T. Ellis, Joseph G. Tischler, Colin R. Woods, Alexander J. Giles, Minghui Hong, Kenji Watanabe, Takashi Taniguchi, Stefan A. Maier, and Kostya S. Novoselov. Sub-diffractive volume-confined polaritons in the natural hyperbolic material hexagonal boron nitride. *Nat. Commun.*, 5(1):5221, 2014.
- [2]Norman Ricker. Further developments in the wavelet theory of seismogram structure. *Bulletin of the Seismological Society of America*, 33(3):197–228, 1943.
- [3]DE Merewether, R. Fisher, and FW Smith. On implementing a numeric huygen's source scheme in a finite difference program to illuminate scattering bodies. *IEEE Trans. Nucl. Sci.*, 27(6):1829–1833, 1980.
- [4]Branko D Gvozdic and Dusan Z Djurdjevic. Performance advantages of cpml over upml absorbing boundary conditions in fdtd algorithm. *J. Electr. Eng.*, 68(1):47–53, 2017.
- [5]Zachary S Sacks, David M Kingsland, Robert Lee, and Jin-Fa Lee. A perfectly matched anisotropic absorber for use as an absorbing boundary condition. *IEEE Trans. Antennas Propag.*, 43(12):1460–1463, 1995.
- [6]Raymond C. Rumpf. Formulation of Plane Wave Expansion Method, EMPossible, 2020. [Online; accessed 7-July-2021].
- [7]Anshuman Kumar, Tony Low, Kin Hung Fung, Phaedon Avouris, and Nicholas X. Fang. Tunable lightmatter interaction and the role of hyperbolicity in graphenehbn system. *Nano Lett.*, 15(5):3172–3180, 2015.
- [8]Yuyu Jiang, Xiao Lin, Tony Low, Baile Zhang, and Hongsheng Chen. Group-velocity-controlled and gate-tunable directional excitation of polaritons in graphene-boron nitride heterostructures. *Laser Photonics Rev.*, 12(5):1800049, 2018.
- [9]Arkadiusz Ciesielski, Lukasz Skowronski, Marek Trzcinski, Ewa Grecka, Pawe Trautman, and Tomasz Szoplik. Evidence of germanium segregation in gold thin films. *Surf. Sci.*, 674:73–78, 2018.
- [10]Dennis M. Sullivan. Z-transform theory and the fdtd method. *IEEE Trans. Antennas Propag.*, 44(1):28–34, 1996.
- [11]Dennis M. Sullivan. *Electromagnetic Simulation Using the FDTD Method, Second Edition*. Wiley, 2013.
- [12]H.A. MacLeod. *Thin-Film Optical Filters*. CRC Press, 2001.
- [13]Weiwei Wan, Xiaodong Yang, and Jie Gao. Strong coupling between mid-infrared localized plasmons and phonons. *Opt. Express*, 24(11):12367–12374, May 2016.
- [14]Peak positions were initially found using a naive peak finding algorithm that sequentially determined all local maxima. This procedure was validated by comparing to a fit to multiple Gaussian functions, although the latter approach would fail in regions where multiple peaks and shoulders were close in frequency. In the case of the inflections in the vicinity of the TO frequency side peaks or shoulders were determined by calculating the second derivative of the spectrum; the resulting curve was then multiplied by -1 and the above peak finding algorithm reapplied.
- [15]R. W. Wood. On a remarkable case of uneven distribution of light in a diffraction grating spectrum. *Lond. Edinb. Dublin Philos. Mag. J. Sci.*, 4:396402, 1902.
- [16]L. Rayleigh. On the dynamical theory of gratings. *Proc. R. Soc. Lond. A.*, 79:399416, 1907.
- [17]H. Gao, J. M. McMahon, M. H. Lee, J. Henzie, S. K. Gray, G. C. Schatz, and T. W. Odom. Rayleigh anomaly-surface plasmon polariton resonances in palladium and gold subwavelength hole arrays. *Opt. Express*, 17:23342340, 2009.
- [18]Angela E. Klein, Norik Janunts, Michael Steinert, Andreas Tünnermann, and Thomas Pertsch. Polarization-resolved near-field mapping of plasmonic aperture emission by a dual-snoms system. *Nano. Lett.*, 14:50105015, 2014.
- [19]S Dai, Z Fei, Q Ma, AS Rodin, M Wagner, AS McLeod, MK Liu, W Gannett, W Regan, and K Watanabe. Tunable phonon polaritons in atomically thin van der waals crystals of boron nitride. *Science*, 343(6175):1125–1129, 2014.
- [20]D.J.T Heneghan, W. M. Dennis, 2021, *Journal TBD*, Vol. TBD, No. TBD. Reprinted here with permission of publisher and authors.
- [21]KB Polypygo. Physical properties of a rock salt lattice made up of deformable ions. *Zh. Eksp. Teor. Fiz.*, 20:497–509, 1950.
- [22]K. U. N. Huang. Lattice vibrations and optical waves in ionic crystals. *Nature*, 167(4254):779–780, 1951.
- [23]A. J. Huber, B. Deutsch, L. Novotny, and R. Hillenbrand. Focusing of surface phonon polaritons. *Appl. Phys. Lett.*, 92(20):203104, 2008.
- [24]William L. Barnes, Alain Dereux, and Thomas W. Ebbesen. Surface plasmon subwavelength optics. *Nature*, 424(6950):824–830, 2003.
- [25]R. H. Ritchie. Plasma losses by fast electrons in thin films. *Phys. Rev.*, 106(5):874–881, 1957.
- [26]David Pines and David Bohm. A collective description of electron interactions: II. collective vs individual particle aspects of the interactions. *Phys. Rev.*, 85(2):338–353, 1952.
- [27]John Pendry. Playing tricks with light. *Science*, 285(5434):1687–1688, 1999.
- [28]R. Estevam da Silva, R. Macdo, T. Dumelow, J. A. P. da Costa, S. B. Honorato, and A. P. Ayala. Far-infrared slab lensing and subwavelength imaging in crystal quartz. *Phys. Rev. B*, 86(15):155152, 2012.
- [29]Nicholas Fang, Hyesog Lee, Cheng Sun, and Xiang Zhang. Sub-diffraction-limited optical imaging with a silver superlens. *Science*, 308(5721):534–537, 2005.
- [30]Katrín Kneipp, Yang Wang, Harald Kneipp, Lev T Perelman, Irving Itzkan, Ramachandra R Dasari, and Michael S Feld. Single molecule detection using surface-enhanced raman scattering (sers). *Phys. Rev. Lett.*, 78(9):1667, 1997.
- [31]Chad E Talley, Joseph B Jackson, Chris Oubre, Nathaniel K Grady, Christopher W Hollars, Stephen M Lane, Thomas R Huser, Peter Nordlander, and Naomi J Halas. Surface-enhanced raman scattering from individual au nanoparticles and nanoparticle dimer substrates. *Nano. Lett.*, 5(8):1569–1574, 2005.
- [32]Daniel Rodrigo, Odeta Limaj, Davide Janner, Dordaneh Etezadi, F. Javier Garca de Abajo, Valerio Pruneri, and Hatice Altug. Mid-infrared plasmonic biosensing with graphene. *Science*, 349(6244):165–168, 2015.
- [33]Alireza Fali, Samuel T. White, Thomas G. Folland, Mingze He, Neda A. Aghamiri, Song Liu, James H. Edgar, Joshua D. Caldwell, Richard F. Haglund, and Yohannes Abate. Refractive index-based control of hyperbolic phonon-polariton propagation. *Nano. Lett.*, 19(11):7725–7734, 2019.
- [34]DE Chang, Anders Sndberg Srensen, PR Hemmer, and MD Lukin. Quantum optics with surface plasmons. *Phys. Rev. Lett.*, 97(5):053002, 2006.
- [35]A Gonzalez-Tudela, Diego Martin-Cano, Esteban Moreno, Luis Martin-Moreno, C Tejedor, and Francisco J Garcia-Vidal. Entanglement of two qubits mediated by one-dimensional plasmonic waveguides. *Phys. Rev. Lett.*, 106(2):020501, 2011.
- [36]Ganesh R Bhimanapati, Zhong Lin, Vincent Meunier, Yeon-woong Jung, Judy Cha, Saptarshi Das, Di Xiao, Youngwoo Son, Michael S Strano, and Valentino R Cooper. Recent advances in two-dimensional materials beyond graphene. *ACS Nano.*, 9(12):11509–11539, 2015.
- [37]Frank HL Koppens, Darrick E Chang, and F Javier Garcia de Abajo. Graphene plasmonics: a platform for strong lightmatter interactions. *Nano. Lett.*, 11(8):3370–3377, 2011.

- [38] S. A. Biehs, M. Tschikin, and P. Ben-Abdallah. Hyperbolic metamaterials as an analog of a blackbody in the near field. *Phys. Rev. Lett.*, 109(10):104301, 2012.
- [39] Yu Guo, Ward Newman, Cristian L Cortes, and Zubin Jacob. Applications of hyperbolic metamaterial substrates. *Adv. OptoElectron.*, 2012.
- [40] C. L. Cortes, W. Newman, S. Molesky, and Z. Jacob. Quantum nanophotonics using hyperbolic metamaterials. *J. Opt.*, 14(6):063001, 2012.
- [41] F. Bonaccorso, Z. Sun, T. Hasan, and A. C. Ferrari. Graphene photonics and optoelectronics. *Nat. Photon.*, 4(9):611–622, 2010.
- [42] Zubin Jacob, Igor I. Smolyaninov, and Evgenii E. Narimanov. Broadband purcell effect: Radiative decay engineering with metamaterials. *Appl. Phys. Lett.*, 100(18):181105, 2012.
- [43] Zhaowei Liu, Hyesog Lee, Yi Xiong, Cheng Sun, and Xiang Zhang. Far-field optical hyperlens magnifying sub-diffraction-limited objects. *Science*, 315(5819):1686–1686, 2007.
- [44] A. V. Kretinin, Y. Cao, J. S. Tu, G. L. Yu, R. Jalil, K. S. Novoselov, S. J. Haigh, A. Gholinia, A. Mishchenko, M. Lozada, T. Georgiou, C. R. Woods, F. Withers, P. Blake, G. Eda, A. Wirsig, C. Hucho, K. Watanabe, T. Taniguchi, A. K. Geim, and R. V. Gorbachev. Electronic properties of graphene encapsulated with different two-dimensional atomic crystals. *Nano Lett.*, 14(6):3270–3276, 2014.
- [45] C. R. Dean, A. F. Young, I. Meric, C. Lee, L. Wang, S. Sorgenfrei, K. Watanabe, T. Taniguchi, P. Kim, K. L. Shepard, and J. Hone. Boron nitride substrates for high-quality graphene electronics. *Nat. Nanotechnol.*, 5(10):722–726, 2010.
- [46] C. R. Dean, L. Wang, P. Maher, C. Forsythe, F. Ghahari, Y. Gao, J. Katoch, M. Ishigami, P. Moon, M. Koshino, T. Taniguchi, K. Watanabe, K. L. Shepard, J. Hone, and P. Kim. Hofstadters butterfly and the fractal quantum hall effect in moiré superlattices. *Nature*, 497(7451):598–602, 2013.
- [47] B. Hunt, J. D. Sanchez-Yamagishi, A. F. Young, M. Yankowitz, B. J. LeRoy, K. Watanabe, T. Taniguchi, P. Moon, M. Koshino, P. Jarillo-Herrero, and R. C. Ashoori. Massive dirac fermions and hofstadter butterfly in a van der waals heterostructure. *Science*, 340(6139):1427–1430, 2013.
- [48] G. L. Yu, R. V. Gorbachev, J. S. Tu, A. V. Kretinin, Y. Cao, R. Jalil, F. Withers, L. A. Ponomarenko, B. A. Piot, M. Potemski, D. C. Elias, X. Chen, K. Watanabe, T. Taniguchi, I. V. Grigorieva, K. S. Novoselov, V. I. Falko, A. K. Geim, and A. Mishchenko. Hierarchy of hofstadter states and replica quantum hall ferromagnetism in graphene superlattices. *Nat. Phys.*, 10(7):525–529, 2014.
- [49] F. D. M. Haldane and S. Raghu. Possible realization of directional optical waveguides in photonic crystals with broken time-reversal symmetry. *Phys. Rev. Lett.*, 100(1):013904, 2008.
- [50] S. Raghu and F. D. M. Haldane. Analogs of quantum-hall-effect edge states in photonic crystals. *Phys. Rev. A*, 78(3):033834, 2008.
- [51] Guorui Chen, Aaron L. Sharpe, Patrick Gallagher, Ilan T. Rosen, Eli J. Fox, Lili Jiang, Bosai Lyu, Hongyuan Li, Kenji Watanabe, Takashi Taniguchi, Jeil Jung, Zhiwen Shi, David Goldhaber-Gordon, Yuanbo Zhang, and Feng Wang. Signatures of tunable superconductivity in a trilayer graphene moiré superlattice. *Nature*, 572(7768):215–219, 2019.
- [52] Guorui Chen, Aaron L. Sharpe, Eli J. Fox, Ya-Hui Zhang, Shaoxin Wang, Lili Jiang, Bosai Lyu, Hongyuan Li, Kenji Watanabe, Takashi Taniguchi, Zhiwen Shi, T. Senthil, David Goldhaber-Gordon, Yuanbo Zhang, and Feng Wang. Tunable correlated chern insulator and ferromagnetism in a moiré superlattice. *Nature*, 579(7797):56–61, 2020.
- [53] K. S. Novoselov, A. Mishchenko, A. Carvalho, and A. H. Castro Neto. 2d materials and van der waals heterostructures. *Science*, 353(6298):aac9439, 2016.
- [54] A. K. Geim and I. V. Grigorieva. Van der waals heterostructures. *Nature*, 499(7459):419–425, 2013.
- [55] Achim Woessner, Mark B. Lundeberg, Yuanda Gao, Alessandro Principi, Pablo Alonso-Gonzlez, Matteo Carrega, Kenji Watanabe, Takashi Taniguchi, Giovanni Vignale, Marco Polini, James Hone, Rainer Hillenbrand, and Frank H. L. Koppens. Highly confined low-loss plasmons in grapheneboron nitride heterostructures. *Nat. Mater.*, 14(4):421–425, 2015.
- [56] Bo Zhao and Zhuomin M. Zhang. Perfect mid-infrared absorption by hybrid phonon-plasmon polaritons in hbn/metal-grating anisotropic structures. *Int. J. Heat Mass Transf.*, 106:1025–1034, 2017.
- [57] Jiong Yang, Mohannad Mayyas, Jianbo Tang, Mohammad B. Ghasemian, Honghua Yang, Kenji Watanabe, Takashi Taniguchi, Qingdong Ou, Lu Hua Li, Qiaoliang Bao, and Kourosh Kalantar-Zadeh. Boundary-induced auxiliary features in scattering-type near-field fourier transform infrared spectroscopy. *ACS Nano*, 14(1):1123–1132, 2020.
- [58] F. J. Alfaro-Mozaz, P. Alonso-Gonzlez, S. Vlez, I. Dolado, M. Autore, S. Mastel, F. Casanova, L. E. Hueso, P. Li, A. Y. Nikitin, and R. Hillenbrand. Nanoimaging of resonating hyperbolic polaritons in linear boron nitride antennas. *Nat. Commun.*, 8(1):15624, 2017.
- [59] Marta Autore, Peining Li, Irene Dolado, Francisco J. Alfaro-Mozaz, Ruben Esteban, Ainhoa Atxabal, Flix Casanova, Luis E. Hueso, Pablo Alonso-Gonzlez, Javier Aizpurua, Alexey Y. Nikitin, Sal Vlez, and Rainer Hillenbrand. Boron nitride nanoresonators for phonon-enhanced molecular vibrational spectroscopy at the strong coupling limit. *Light Sci. Appl.*, 7(4):17172–17172, 2018.
- [60] T. G. Folland, A. Fali, S. T. White, J. R. Matson, S. Liu, N. A. Aghamiri, J. H. Edgar, R. F. Haglund, Y. Abate, and J. D. Caldwell. Reconfigurable infrared hyperbolic metasurfaces using phase change materials. *Nat. Commun.*, 9(1):4371, 2018.
- [61] Fei Cheng, Xiaodong Yang, and Jie Gao. Ultrasensitive detection and characterization of molecules with infrared plasmonic metamaterials. *Sci. Rep.*, 5(1):14327, 2015.
- [62] Yee Kane. Numerical solution of initial boundary value problems involving maxwell's equations in isotropic media. *IEEE Trans. Antennas Propag.*, 14(3):302–307, 1966.
- [63] A. Tafove and S.C. Hagness. *Computational Electrodynamics: The Finite-difference Time-domain Method*. Artech House, 2005.
- [64] PGI Compilers and Tools: OpenACC Getting Started Guide, NVIDIA, 11/19/2020 2020.
- [65] Edward D. Palik. *Handbook of optical constants of solids*. Academic Press, Orlando, 1985.
- [66] Jun John Sakurai and Jim Napolitano. *Modern Quantum Mechanics*. Cambridge University Press, 2017.
- [67] D.J.T Heneghan, W. M. Dennis, 2021, *Journal TBD*, Vol. TBD, No. TBD. Reprinted here with permission of publisher and authors.

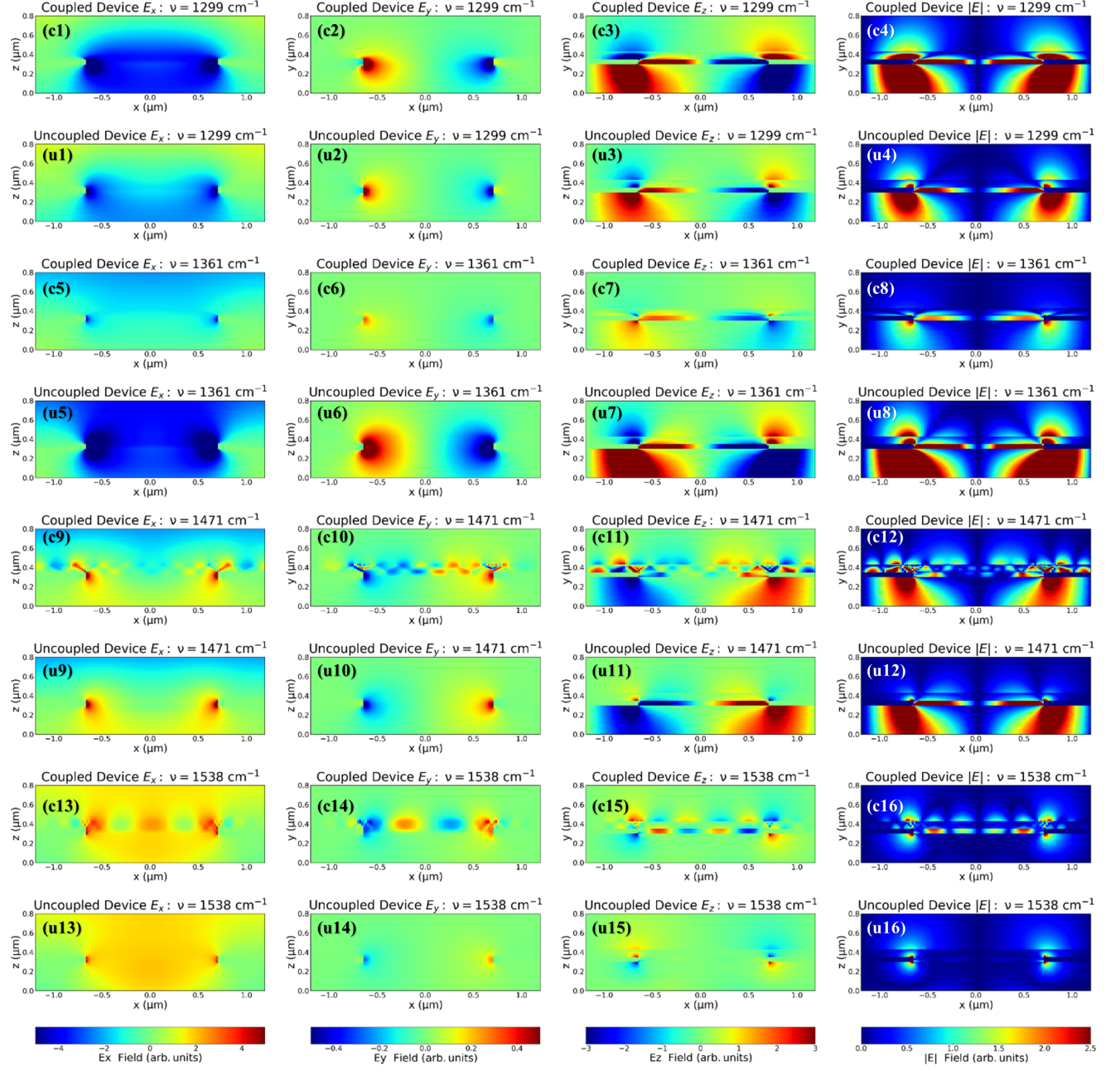


FIG. 11: Cross-sectional colormaps of the field components in both the hBN (coupled) devices and uncoupled devices at four representative frequencies

Cross-sectional colormaps of the field components in both the hBN (coupled) devices and uncoupled devices at four representative frequencies. Panes (c1), (c2), (c3), and (c4) show the field in the hBN (coupled) device at monitored at 1298 cm^{-1} . Panes (u1), (u2), (u3), and (u4) show the field in the uncoupled device at the same frequency. The remaining 16 panes follow the same ordering scheme but for monitoring frequencies of 1361 , 1471 and 1538 cm^{-1} , respectively.

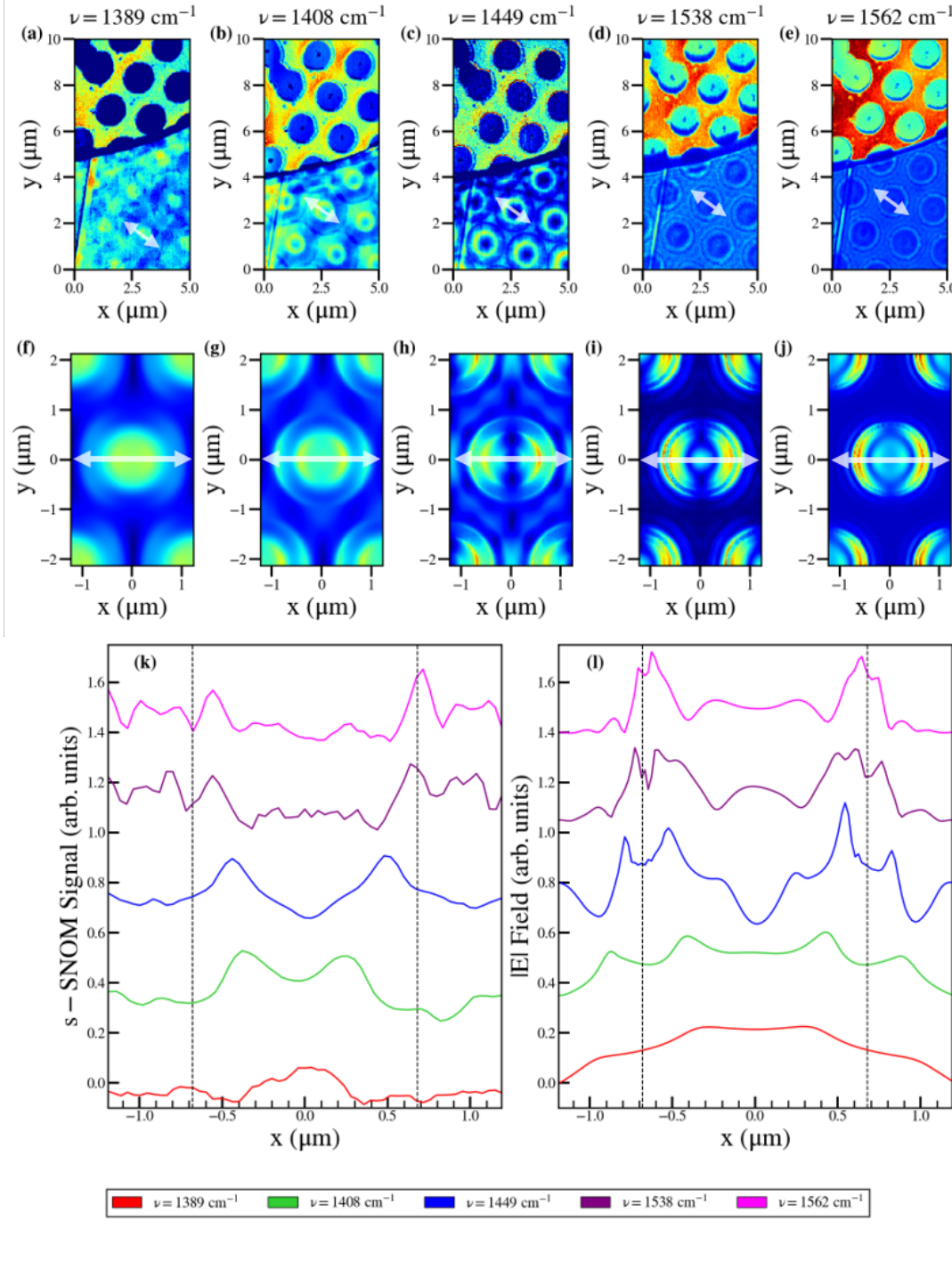


FIG. 12: Experimental and simulational planar colormaps and their central lineout data.

(a), (b), (c), (d) and (e) Experimental s-SNOM images monitored at 1389, 1408, 1449, 1538 and 1562 cm^{-1} , respectively. (f), (g), (h), (i) and (j) Plots of the magnitude if the electric field at the vacuum/hBN interface monitored at 1266, 1408, 1449, and 1538 cm^{-1} , respectively. (k) Line-out data from the s-SNOM data plotted as a function of position across the line indicated in (a) - (e). (l) Line-out data from the magnitude of the electric field data plotted along the line in (f) - (j). The dashed lines in (l) and (k) represent the position of the cavity beneath the hBN layer. All data in this figure were individually scaled for greater ease of comparison.